iScience

CellPress
OPEN ACCESS

Article

Tmem30a protects against podocyte injury through suppression of pyroptosis

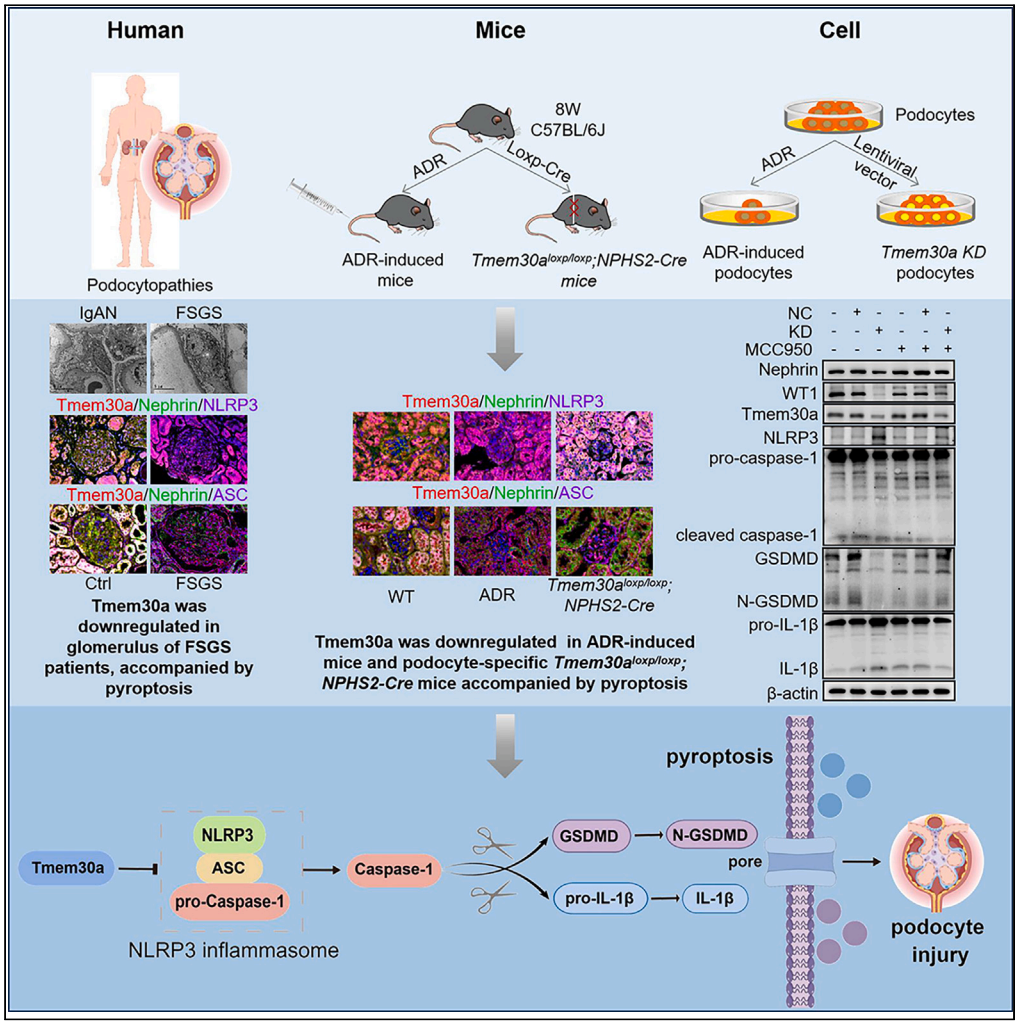

Yanpei Hou, Sipei Chen, Lei Peng, ..., Li Wang, Yi Li, Guisen Li

liyisn@med.uestc.edu.cn (Y.L.)
guisenli@163.com (G.L.)

Highlights

Tmem30a was downregulated in FSGS patients and ADR-induced podocyte injury models

Loss of Tmem30a expression induces podocyte injury by activating pyroptosis

MCC950 and DSF alleviates podocyte injury by inhibiting pyroptosis

Hou et al., iScience 27, 109976
June 21, 2024
https://doi.org/10.1016/j.isci.2024.109976

iScience

CellPress
OPEN ACCESS

Article

Tmem30a protects against podocyte injury through suppression of pyroptosis

Yanpei Hou,[1] Sipei Chen,[1] Lei Peng,[1] Liming Huang,[1] Huijian Zhang,[1] Ping Zhang,[1] Min Yu,[1] Lin Xiong,[1] Xiang Zhong,[1] Wenjing Liu,[2] Xianjun Zhu,[2] Li Wang,[1] Yi Li,[1,3,*] and Guisen Li[1,3,4,*]

SUMMARY

Podocytopathies, such as focal segmental glomerulosclerosis (FSGS), are characterized by podocyte injury and can easily progress to end-stage kidney disease. However, the mechanisms underlying podocyte injury remain unclear. We observed podocyte injury along with pyroptosis in patients with FSGS. Bioinformatic analysis of public datasets revealed that transmembrane protein 30a (Tmem30a) might be associated with FSGS. The expression of Temem30a and the podocyte-related protein, nephrin, were significantly downregulated in patients with FSGS, adriamycin (ADR)-induced mice, and podocyte-specific *Tmem30a*$^{loxP/loxP}$*; NPHS2-Cre* mice, whereas the expression of NLR family pyrin domain containing 3 (NLRP3) and ASC, two pyroptosis-related proteins, were significantly upregulated. Meanwhile, the pyroptosis inhibitor MCC950 and disulfiram (DSF) increased Tmem30a and podocyte-related proteins expression, and inhibited pyroptosis-related proteins expression in ADR-induced mouse podocytes and *Tmem30a* knockdown (KD) mouse podocytes. Therefore, Tmem30a might protect against podocyte injury by inhibiting pyroptosis, suggesting a potential therapeutic target for podocytopathies.

INTRODUCTION

Podocytopathies are kidney diseases in which direct or indirect podocyte injury causes proteinuria or nephrotic syndrome, which can easily progress to end-stage kidney disease.[1] Focal segmental glomerulosclerosis (FSGS), minimal change disease, membranous nephropathy, and diabetic nephropathy commonly accompany typical podocyte injury. The prevalence of podocytopathies is increasing worldwide, which places a considerable economic burden on national medical systems and the families of patients.[2] Podocyte injury is characterized by fissure diaphragm abnormalities, podocyte loss, loss of negative charge, glomerular basement membrane (GBM) destruction, GBM malformation, and podocyte-associated endothelial cell dysfunction.[3] Additionally, the expression of key podocyte-associated molecules, including Wilms tumor 1 (WT1), nephrin, podocin, and synaptopodin, are significantly lower in the podocytes of patients with FSGS than in those without.[4] However, the underlying mechanisms of podocyte injury remain unclear. Elucidating these mechanisms could help identify potential therapeutic targets and improve the diagnosis and treatment of podocytopathies.

Transmembrane protein 30a (Tmem30a), the β-subunit of P4-ATPases, is widely expressed in mammals. Tmem30a plays an important role in maintaining the asymmetric distribution of phospholipids in cell membranes, intracellular vesicle transport, signal transduction, blood coagulation, cell migration and polarization, and cell apoptosis by interacting with 11 types of P4-ATPase.[5–7] Tmem30a deficiency can cause retinal bipolar cell apoptosis, anemia, cerebellar ataxia, and reduced angiogenesis.[8–11] Moreover, our previous study showed that podocyte-specific *Tmem30a*$^{loxP/loxP}$*; NPHS2-Cre* mice exhibited albuminuria, podocyte damage and loss, and mesangial cell proliferation with substantial extracellular matrix accumulation, which eventually developed into FSGS.[12] However, the specific effects and mechanisms of Tmem30a in podocyte injury remain unclear.

Tmem30a and P4-ATPase form heterodimers crucial to the maturation of P4-ATPase from the endoplasmic reticulum to other membrane organelles. When Tmem30a function is impaired, the interacting P4-ATPase remains in the endoplasmic reticulum and cannot maintain the asymmetric distribution of phospholipids on both sides of the membrane, leading to phosphatidylserine exposure on the cell surface.[13] Annexin V binds to phosphatidylserine and participates in pyroptosis.[14] Pyroptosis is a pro-inflammatory programmed cell death, mediated by the gasdermin family of proteins and is characterized by continuous cell swelling until the cell membrane perforates and ruptures, thereby releasing the cell contents and inducing an intense inflammatory stress response.[15–17] The NLR family pyrin domain containing 3 (NLRP3) inflammasome consists of NLRP3, adaptor ASC, and pro-caspase-1. Caspase 1 is activated within the inflammasome, and activated caspase-1

[1]Department of Nephrology, Sichuan Provincial People's Hospital, University of Electronic Science and Technology of China, Sichuan Clinical Research Center for Kidney Diseases, Chengdu 610072, China
[2]Sichuan Provincial Key Laboratory for Human Disease Gene Study, Center for Medical Genetics, Sichuan Provincial People's Hospital, University of Electronic Science and Technology of China, Chengdu 610072, China
[3]These authors contributed equally
[4]Lead contact
*Correspondence: liyisn@med.uestc.edu.cn (Y.L.), guisenli@163.com (G.L.)
https://doi.org/10.1016/j.isci.2024.109976

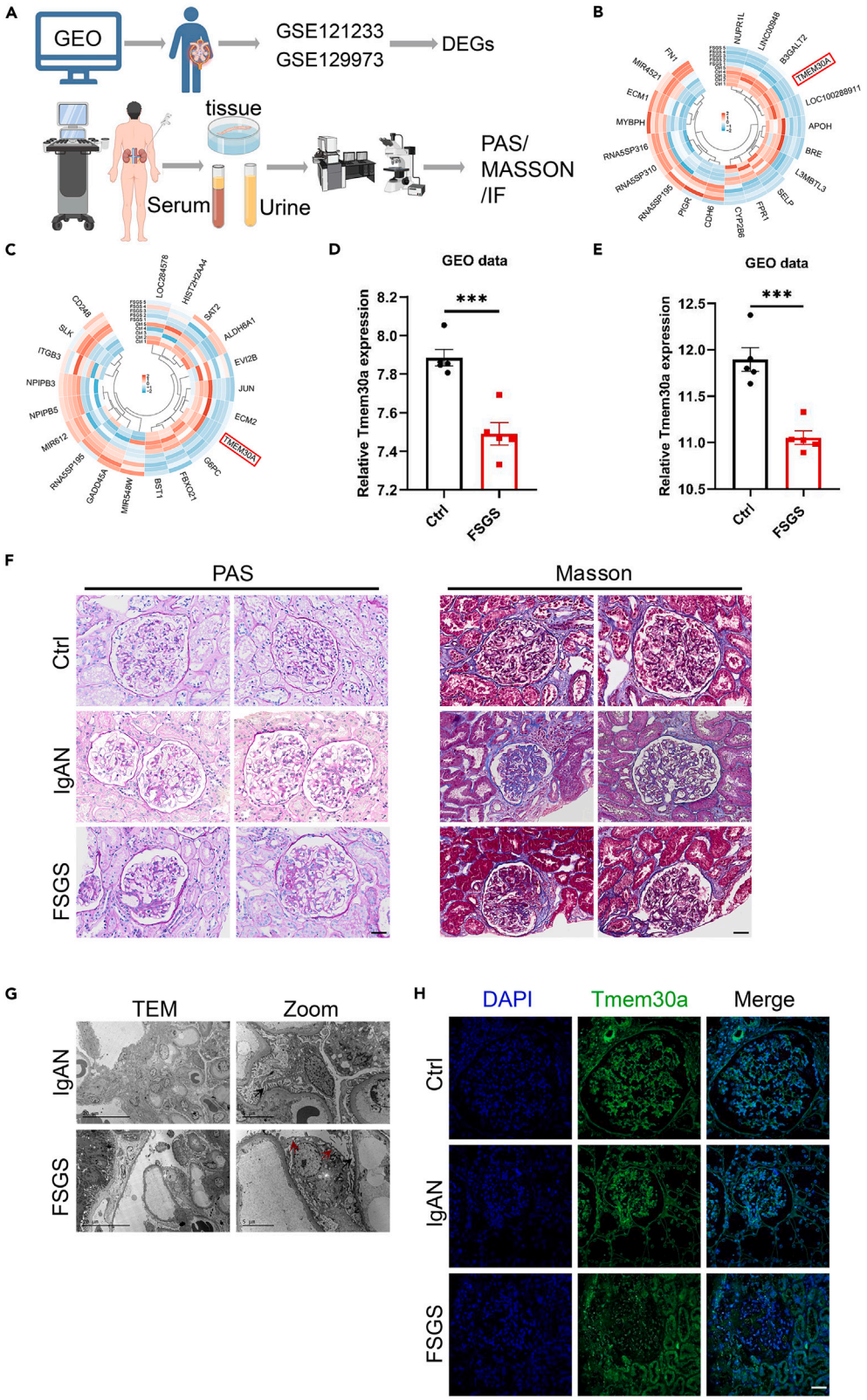
A
GEO
GSE121233
GSE129973
DEGs
tissue
Serum
Urine
PAS/
MASSON
/IF
B
C
D
GEO data
Relative Tmem30a expression
***
Ctrl
FSGS
E
GEO data
Relative Tmem30a expression
***
Ctrl
FSGS
F
PAS
Masson
Ctrl
IgAN
FSGS
G
TEM
Zoom
IgAN
FSGS
H
DAPI
Tmem30a
Merge
Ctrl
IgAN
FSGS

Figure 1. Tmem30a expression in patients with FSGS and controls

(A) Overview of the bioinformatics analysis flow and collected renal tissues from clinical patients.

(B and C) Heatmap of DEGs between the FSGS and Ctrl groups in the GSE121233 and GSE129973 datasets.

(D and E) Tmem30a expression levels in FSGS and Ctrl groups in the GSE121233 and GSE129973 datasets. n = 5/group. Data are represented as mean ± SEM.

(F) PAS and Masson's trichrome staining of kidney tissue in FSGS group, IgAN group, and Ctrl group (scale bar: 20 μm).

(G) Transmission electron microscopy images of kidney tissues in patients with FSGS and IgAN. Black arrowheads: foot process; red arrowheads: membrane disruption.

(H) Immunofluorescence images of Tmem30a expression in glomerular of FSGS group, IgAN group, and Ctrl group (scale bar: 20 μm). DEG, differentially expressed gene; Ctrl, control; FSGS, focal segmental glomerulosclerosis; IgAN, IgA nephropathy; PAS, periodic acid-Schiff; Tmem30a, transmembrane protein 30a. ***$p < 0.001$.

cleaves gasdermin D (GSDMD). Simultaneously, caspase-1 cleaves pro-IL-1β and pro-IL-18 into their activated forms. Upon permeabilization of the plasma membrane by GSDMD pores, cells undergo pyroptosis that promotes the release of mature IL-1β and IL-18.[15,18–24] Pyroptosis may play an important role in the pathogenesis and progression of nephropathies. GSDMD-mediated pyroptosis is crucial in the occurrence and development of acute kidney injury induced by cisplatin.[25] NLRP3 activation-driven pyroptosis is involved in lupus nephritis, and human immunodeficiency virus-associated nephropathy.[26,27] Therefore, we hypothesize that Tmem30a participates in podocyte injury by mediating pyroptosis.

Accordingly, this study aimed to elucidate the role of Tmem30a involving pyroptosis in podocyte injury.

RESULTS

Tmem30a is downregulated in patients with FSGS

To identify the key genes involved in podocyte injury, we performed bioinformatic analysis of FSGS-related datasets in the Gene Expression Omnibus (GEO) database and collected clinical renal biopsy tissues for validation (Figure 1A). The GSE121233 and GSE129973 datasets were downloaded to identify differentially expressed genes (DEGs) between the control and FSGS kidney tissue (criteria: fold change ≥ |1.2| and adjusted $p < 0.05$). Heatmaps were generated from the DEGs obtained from the GSE121233 and GSE129973 datasets (Figures 1B and 1C). Tmem30a expression was significantly reduced in the glomeruli of kidney samples from patients with FSGS (Figures 1D and 1E).

Additionally, we collected kidney tissues from ten patients with primary FSGS, five patients with non-segmental glomerulosclerosis IgA nephropathy (IgAN), and five normal kidney tissues near cancer sites. Figure 1F presents the periodic acid-schiff (PAS) and Masson's trichrome staining results of FSGS, IgAN, and control kidney tissues. Transmission electron microscopy revealed the disappearance and extensive fusion of podocytes, along with signs of pyroptosis, such as pore formation in the membranes of podocytes, in the FSGS group compared to the IgAN group (Figure 1G). Furthermore, immunofluorescence assay showed a significant decrease in Tmem30a expression in the FSGS group compared with that in the IgAN and control groups (Figure 1H).

Tmem30a is downregulated in adriamycin-induced podocyte injury

To examine the function of Tmem30a in podocyte injury *in vivo*, a murine model of podocyte injury was induced via tail vein injection of adriamycin (ADR) (Figure 2A). PAS staining showed proliferated mesangial cell matrix and widened mesangial region in the ADR group compared to the control group (Figure 2B). Urinary albumin/creatinine levels were also significantly higher in the ADR group than those in the control group (Figure 2C). After testing for proteinuria and evaluating the pathological characteristics of the kidneys in the ADR-induced mice, we analyzed the effects of ADR on the ultrastructure of podocytes using transmission electron microscopy. The disappearance and extensive fusion of podocytes were observed in the ADR-induced mice compared to the control mice (Figure 2D). Notably, immunohistochemical assay showed a decrease in Tmem30a expression in the ADR group compared with that in the control group (Figure 2E).

Next, mouse podocytes were treated with different concentrations of ADR for varying durations to generate an *in vitro* model of podocyte injury (Figure 2A). Cell counting kit-8 (CCK-8) assay showed that ADR treatment for 24 and 48 h dose-dependently decreased the viability of mouse podocytes (Figure 2F). Therefore, based on safety and effectiveness, we selected 0.4 μg/mL of ADR and a 24-h duration for the subsequent experiments. Furthermore, western blotting showed a significant decrease in Tmem30a expression in the ADR group, along with a decrease in the expression of the podocyte-related proteins nephrin and WT1 compared to those in the control group (Figures 2G–2J).

Loss of Tmem30a expression induces podocyte injury

To further investigate the role of Tmem30a in podocyte injury, we constructed a Tmem30a knockout/knockdown (KD) model (Figure 3A). The podocyte-specific *Tmem30a*$^{loxP/loxP}$*; NPHS2-Cre* mouse model was constructed using the *NPHS2-Cre* cell line. PAS staining of kidney sections revealed severe mesangial cell proliferation with extracellular matrix deposition, capsular synechia, and presented pathological features of FSGS (Figure 3B). Immunofluorescence staining showed decreased Tmem30a expression in the glomerulus of *Tmem30a*$^{loxP/loxP}$*; NPHS2-Cre* mice compared to the wild-type (WT) mice (Figure 3C).

In vitro, Tmem30a was knocked down in immortalized mouse podocyte lines using lentivirus-mediated RNA interference. Real-time polymerase chain reaction (real-time PCR) confirmed that the Tmem30a knockdown efficiency was about 50% (Figure 3D). Western blotting confirmed significantly decreased Tmem30a expression in *Tmem30a* KD mouse podocytes, as well as decreased nephrin and WT1 expression (Figures 3E–3H).

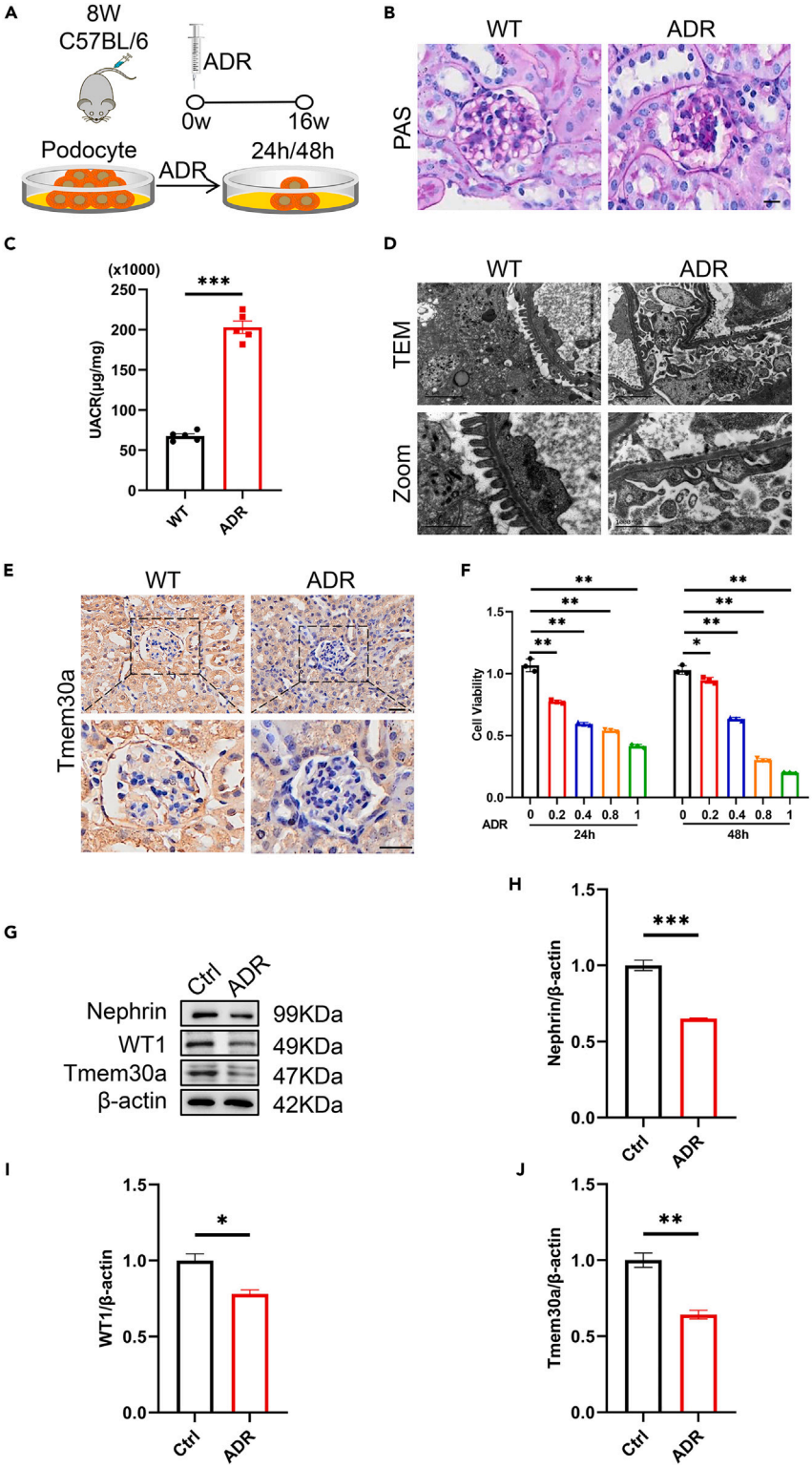

Figure 2. Tmem30a expression levels in mice and cell models of ADR-induced podocyte injury

(A) Construction of the ADR-induced mice and cell models.

(B) PAS staining of kidney tissue in ADR-induced mice and WT mice (scale bar: 20 μm).

(C) UACR levels in ADR-induced mice and WT mice. *n* = 5/group. Data are represented as mean ± SEM.

Figure 2. *Continued*

(D) Transmission electron microscopy images of glomeruli in ADR-induced mice and WT mice.

(E) Representative images of immunohistochemical staining for Tmem30a in ADR-induced mice and WT mice (scale bar: 20 μm).

(F) ADR was used at different concentrations and time points to observe mouse podocyte viability. n = 3/group. Data are represented as mean ± SEM.

(G) The expression of Tmem30a, nephrin, and WT1 in ADR-induced mouse podocytes and normal mouse podocytes using western blotting.

(H–J) Immunoblot quantification of nephrin, WT1, and Tmem30a in (G). n = 3/group. Data are represented as mean ± SEM. ADR, adriamycin; WT, wild type; Ctrl, control; PAS, periodic acid-Schiff; Tmem30a, transmembrane protein 30a; UACR, urinary albumin/creatinine ratio; WT1, Wilms tumor 1. *$p < 0.05$, **$p < 0.01$, ***$p < 0.001$.

MCC950 alleviates podocyte injury by inhibiting ADR-induced pyroptosis

To verify the relationship between podocyte injury and pyroptosis, we retrieved relevant datasets from the GEO database and constructed ADR-induced mouse podocytes (Figure 4A). The GSE124622 dataset was downloaded from the GEO database to identify DEGs between normal and ADR-induced human podocytes. DEGs involved in pyroptosis were significantly upregulated in ADR-induced human podocytes compared to those in normal human podocytes (Figure 4B). In addition, a CCK-8 assay was performed to examine the viability of ADR-injured mouse podocytes after the NLRP3 inhibitor MCC950 treatment. Expectedly, 24-h ADR treatment decreased mouse podocyte viability, which was significantly reversed by 48-h MCC950 treatment (Figure 4C).

Western blot analysis revealed that Tmem30a, nephrin, and WT1 expression decreased in ADR-induced mouse podocytes compared to those in the control group; however, MCC950 treatment reversed this trend (Figures 4D–4G). Additionally, we examined the expression of several pyroptosis-related proteins, including NLRP3, pro-caspase-1, cleaved caspase-1, GSDMD, N-GSDMD, pro-IL-1β, and IL-1β. Compared to those in the control group, NLRP3, N-GSDMD/GSDMD, cleaved caspase-1/pro-caspase-1, and IL-1β/pro-IL-1β protein expression levels were upregulated in the ADR group, suggesting that ADR stimulation induced pyroptosis in mouse podocytes (Figures 4D and 4H–4K). However, MCC950 treatment suppressed ADR-induced NLRP3 inflammasome activation, as evidenced by a decrease in the protein expression of NLRP3, N-GSDMD/GSDMD, cleaved caspase-1/pro-caspase-1 and IL-1β/pro-IL-1β (Figures 4D and 4H–4K). These results indicate that pyroptosis occurs during podocyte injury and that MCC950 alleviates podocyte pyroptosis.

Disulfiram alleviates podocyte injury by inhibiting ADR-induced pyroptosis

To confirm whether the GSDMD inhibitor disulfiram (DSF) could inhibit ADR-induced pyroptosis *in vitro*, we tested the protein expression levels of NLRP3, pro-caspase-1, cleaved caspase-1, GSDMD, N-GSDMD, pro-IL-1β, and IL-1β in the podocytes exposed to ADR with or without DSF (Figure 5A). Then, we measured the effect of DSF on podocytes viability using CCK-8 assay and found that DSF treatment could partially reverse the decreased mouse podocyte viability exposed to ADR (Figure 5B). Western blot analysis revealed that compared with those in the control group, the podocytes exposed to ADR exhibited significantly higher expression levels of NLRP3, N-GSDMD/GSDMD, cleaved caspase-1/pro-caspase-1, and IL-1β/pro-IL-1β. After treatment with DSF, the podocytes exposed to ADR showed a significant reduction in the expression levels of NLRP3, N-GSDMD/GSDMD, cleaved caspase-1/pro-caspase-1, and IL-1β/pro-IL-1β (Figures 5C and 5G–5J). Meanwhile, Tmem30a, nephrin, and WT1 expression decreased in ADR-induced mouse podocytes compared to those in the control group; however, DSF treatment reversed this trend (Figures 5C and 5D–5F). These results indicate that DSF alleviates ADR induced podocyte pyroptosis.

NLRP3 upregulation is observed in patients with FSGS, ADR-induced mice, and podocyte-specific *Tmem30a*$^{loxP/loxP}$; *NPHS2-Cre* mice

The expression of NLRP3, nephrin and Tmem30a in glomerular podocytes of patients with FSGS, ADR-induced mice, and podocyte-specific *Tmem30a*$^{loxP/loxP}$; *NPHS2-Cre* mice were observed by the multiplexed immunofluorescence method (Figure 6A). The fluorescence intensity of NLRP3 increased, and that of Tmem30a and nephrin decreased in the glomerulus of patients with FSGS compared to those in the control group (Figure 6B). Similarly, NLRP3 expression increased, and Tmem30a and nephrin expression decreased in glomerulus from ADR-treated mice compared to those in the control group, with partial colocalization of the three proteins (Figure 6C). Additionally, NLRP3 expression was significantly upregulated in the kidney tissues of podocyte-specific *Tmem30a*$^{loxP/loxP}$; *NPHS2-Cre* mice compared to that of the control group, with partial colocalization with nephrin (Figure 6D).

ASC upregulation is observed in patients with FSGS, ADR-induced mice, and podocyte-specific *Tmem30a*$^{loxP/loxP}$; *NPHS2-Cre* mice

The multiplexed immunofluorescence method was used to observe the expression of ASC, nephrin, and Tmem30a in glomerular podocytes of patients with FSGS, ADR-induced mice, and podocyte-specific *Tmem30a*$^{loxP/loxP}$; *NPHS2-Cre* mice (Figure 7A). The fluorescence intensity of ASC increased, and that of Tmem30a and nephrin decreased in the glomerulus of patients with FSGS and ADR-treated mice, compared to those in the control group, with partial colocalization of the three proteins (Figures 7B and 7C). Additionally, ASC expression was significantly upregulated in the glomerulus of podocyte-specific *Tmem30a*$^{loxP/loxP}$; *NPHS2-Cre* mice compared to those in the control group, with partial colocalization with nephrin (Figure 7D).

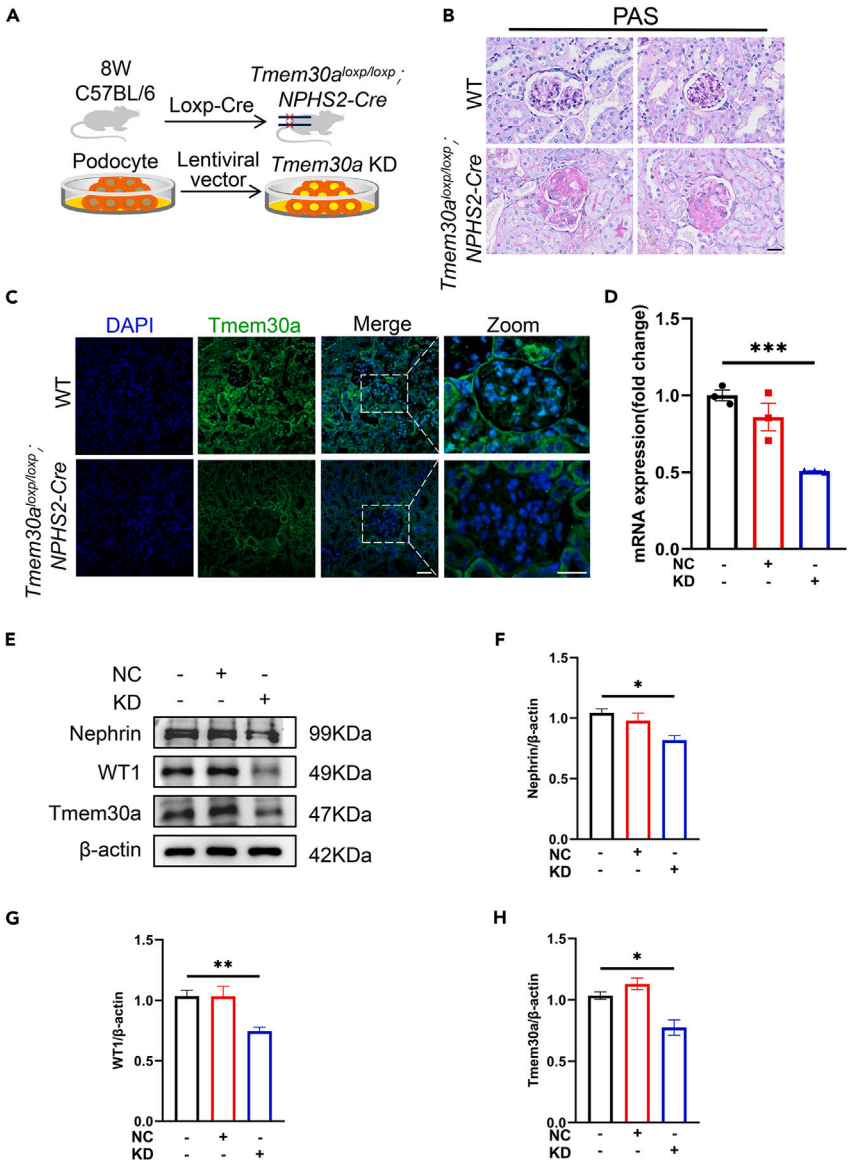

Figure 3. Construction of podocyte-specific *Tmem30a*$^{loxP/loxP}$; *NPHS2-Cre* mice and *Tmem30a* KD mouse podocytes

(A) Flowchart of the construction of podocyte-specific *Tmem30a*$^{loxP/loxP}$; *NPHS2-Cre* mice and *Tmem30a* KD mouse podocytes.

(B) PAS staining of kidney sections in *Tmem30a*$^{loxP/loxP}$; *NPHS2-Cre* mice and WT mice (scale bar: 20 μm).

(C) Representative immunofluorescence staining images of Tmem30a in kidney samples from *Tmem30a*$^{loxP/loxP}$; *NPHS2-Cre* mice and WT mice (scale bar: 20 μm).

(D) Real-time PCR showing the relative mRNA expression of Tmem30a in the Ctrl group, NC group and *Tmem30a* KD group *in vitro*. n = 3/group. Data are represented as mean ± SEM.

(E) The expression of nephrin, WT1, and Tmem30a in the Ctrl group, NC group and *Tmem30a* KD group using western blotting.

(F–H) Immunoblot quantification of nephrin, WT1, and Tmem30a in (E). n = 3/group. Data are represented as mean ± SEM. Ctrl, control; NC, negative control; KD, knockdown; Real-time PCR, reverse-transcription polymerase chain reaction; Tmem30a, transmembrane protein 30a; WT, wild type; WT1, Wilms tumor 1. *$p < 0.05$; **$p < 0.01$; ***$p < 0.001$.

ADR aggravated podocyte injury and pyroptosis in *Tmem30a* KD mouse podocytes

To explore the relationship between podocyte injury and pyroptosis, *Tmem30a* KD mouse podocytes were treated with ADR (Figure 8A). We detected the expression levels of NLRP3, pro-caspase-1, cleaved caspase-1, GSDMD, N-GSDMD, pro-IL-1β, and IL-1β in *Tmem30a* KD podocytes and compared them with those in the control group. Notably, the expression levels of NLRP3, N-GSDMD/GSDMD, cleaved caspase-1/pro-caspase-1, and IL-1β/pro-IL-1β expression was increased significantly in *Tmem30a* KD podocytes, confirming that Tmem30a loss causes podocyte pyroptosis (Figures 8B and 8F–8I).

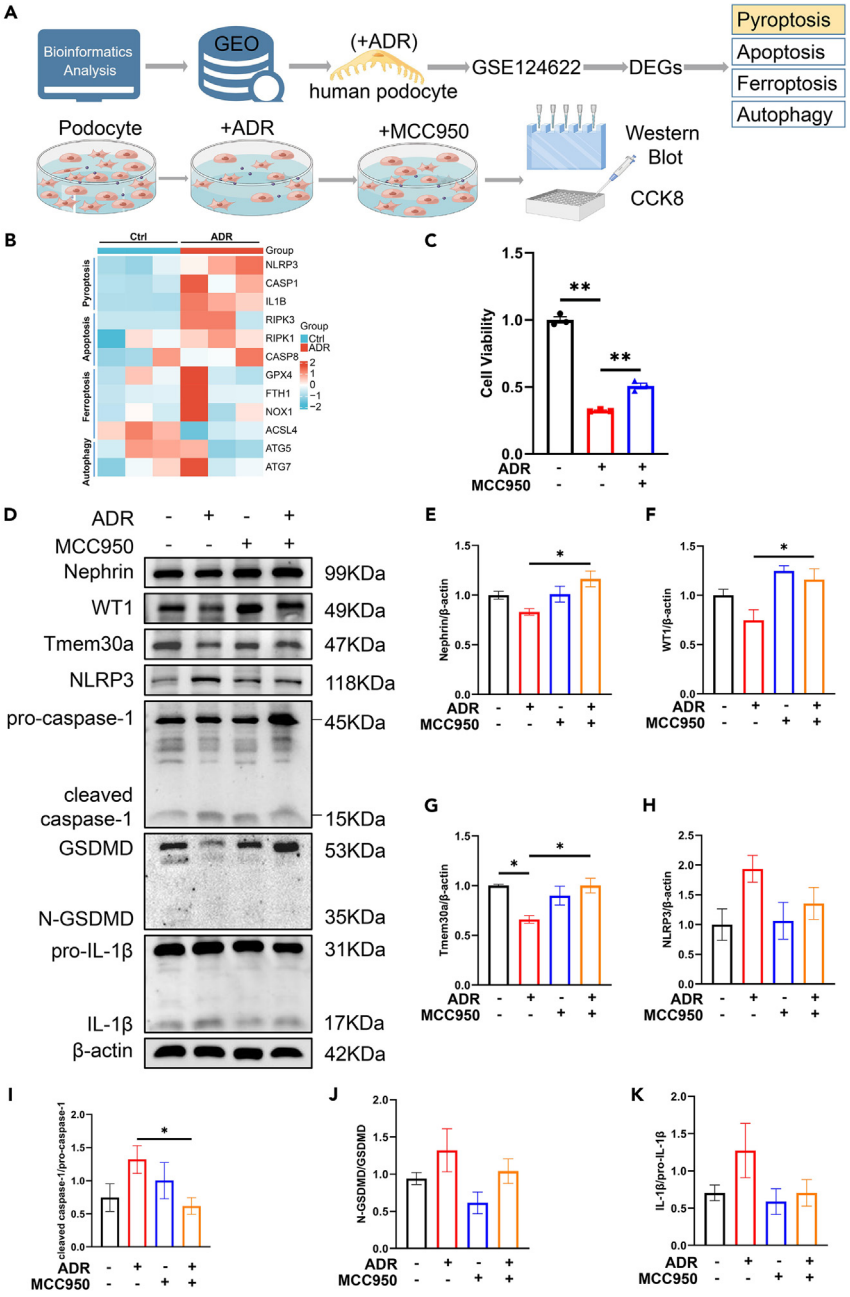

Figure 4. MCC950 alleviates podocyte injury by inhibiting ADR-induced pyroptosis

(A) Bioinformatic analysis flowchart between normal human podocytes and ADR-induced human podocytes, and construct ADR-induced mouse podocytes.

(B) Heatmap of DEGs in ADR-induced human podocytes and normal human podocytes in the GSE124622 dataset.

(C) Cell viability of mouse podocytes after ADR treatment for 24 h and then MCC950 treatment for 48 h. *n* = 3/group. Data are represented as mean ± SEM.

(D) The expression levels of nephrin, WT1, Tmem30a, NLRP3, pro-caspase-1, cleaved caspase-1, GSDMD, N-GSDMD, pro-IL-1β, and IL-1β in the Ctrl group, ADR group, MCC950 group, and ADR+MCC950 group using western blotting.

(E–K) Immunoblot quantification of nephrin, WT1, Tmem30a, NLRP3, cleaved caspase-1/pro-caspase-1, N-GSDMD/GSDMD, and IL-1β/pro-IL-1β in (D). *n* = 3/group. Data are represented as mean ± SEM. ADR, adriamycin; Ctrl, control; DEG, differentially expressed gene; GSDMD, gasdermin D; NLRP3, NLR family pyrin domain containing 3; Tmem30a, transmembrane protein 30a; WT1, Wilms tumor 1. *$p < 0.05$; **$p < 0.01$.

At the same time, ADR was applied to *Tmem30a* KD mouse podocytes, and the pyroptosis-related proteins of NLRP3, N-GSDMD/GSDMD, cleaved caspase-1/pro-caspase-1, and IL-1β/pro-IL-1β expression were significantly increased, while the expression levels of Tmem30a and podocyte-related proteins nephrin and WT1 were decreased (Figures 8B–8I). Collectively, these results showed that ADR

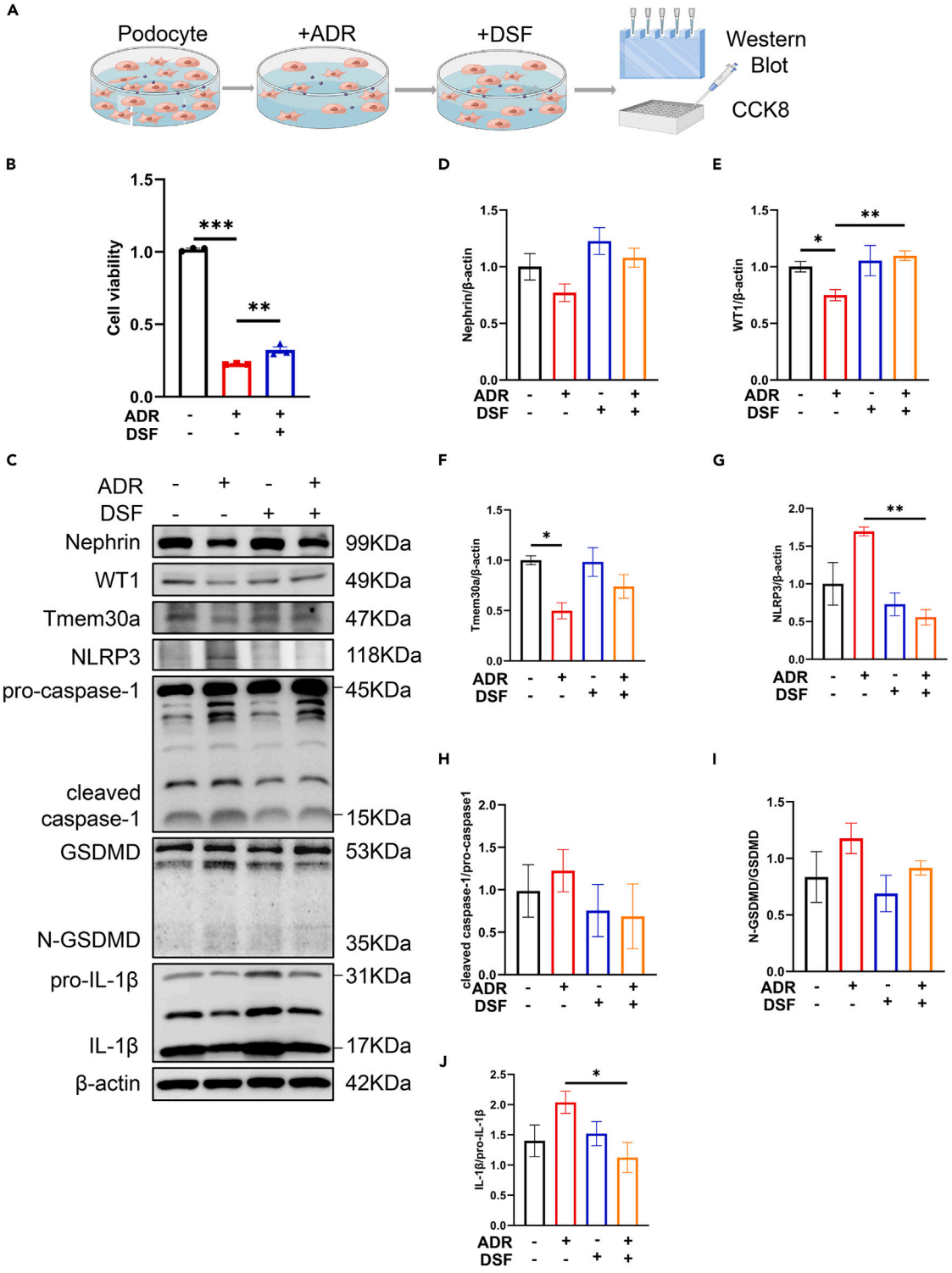

Figure 5. DSF alleviates podocyte injury by inhibiting ADR-induced pyroptosis

(A) Constructed ADR-induced mouse podocytes and treated with DSF.

(B) Cell viability of mouse podocytes after ADR treatment for 24 h and DSF treatment for 1 h. *n* = 3/group. Data are represented as mean ± SEM.

(C) The expression levels of nephrin, WT1, Tmem30a, NLRP3, pro-caspase-1, cleaved caspase-1, GSDMD, N-GSDMD, pro-IL-1β, and IL-1β in the Ctrl group, ADR group, DSF group, and ADR+DSF group using western blotting.

Figure 5. *Continued*

(D–J) Immunoblot quantification of nephrin, WT1, Tmem30a, NLRP3, cleaved caspase-1/pro-caspase-1, N-GSDMD/GSDMD, and IL-1β/pro-IL-1β in (C). n = 3/group. Data are represented as mean ± SEM. ADR, adriamycin; Ctrl, control; GSDMD, gasdermin D; NLRP3, NLR family pyrin domain containing 3; Tmem30a, transmembrane protein 30a; WT1, Wilms tumor 1. *$p < 0.05$; **$p < 0.01$; ***$p < 0.001$.

aggravated podocyte injury and podocyte pyroptosis in *Tmem30a* KD mouse podocytes, indicating that heredity and environment could contribute to podocyte damage by inducing pyroptosis.

MCC950 alleviates podocyte injury by inhibiting pyroptosis in *Tmem30a* KD mouse podocytes

To explore the mechanisms between Tmem30a and pyroptosis, we treated *Tmem30a* KD podocytes with the NLRP3 inhibitor MCC950 to observe changes in podocyte injury and pyroptosis levels (Figure 9A). After MCC950 treatment for 48 h, the *Tmem30a* KD mouse podocytes showed a significant reduction in the expression levels of NLRP3, N-GSDMD/GSDMD, cleaved caspase-1/pro-caspase-1, and IL-1β/pro-IL-1β and a significant increase in the expression levels of Tmem30a, nephrin, and WT1 (Figures 9B–9I). Overall, these results indicated that pyroptosis occurs in *Tmem30a* KD mouse podocytes and that MCC950 alleviates podocyte pyroptosis.

DSF alleviates podocyte injury by inhibiting pyroptosis in *Tmem30a* KD mouse podocytes

We treated *Tmem30a* KD podocytes with the GSDMD inhibitor DSF to observe changes in podocyte injury and pyroptosis levels (Figure 10A). The *Tmem30a* KD mouse podocytes showed a significant reduction in the expression levels of NLRP3, N-GSDMD/GSDMD, cleaved caspase-1/pro-caspase-1, and IL-1β/pro-IL-1β and a significant increase in the expression levels of Tmem30a, nephrin, and WT1 after DSF treatment (Figures 10B–10I). Overall, these results indicated that DSF alleviates podocyte pyroptosis in *Tmem30a* KD mouse podocytes.

DISCUSSION

Podocyte injury plays a vital role in the pathogenesis of podocytopathies, ultimately leading to the breakdown of the glomerular filtration barrier and histological changes. Genetic, immunological, infectious, and toxic factors can cause podocyte injury,[28] and recently, the mechanisms underlying podocyte injury have received considerable attention. An in-depth understanding of the molecules involved in the disease's pathogenesis would facilitate the development of new treatment options. This study demonstrated that Tmem30a inhibits the activation of the NLRP3 inflammasome, reducing podocyte pyroptosis and alleviating podocyte damage (Figure 11).

Our team is dedicated to study the function and mechanism of Tmem30a in kidney diseases. And we constructed the podocyte-specific *Tmem30a*$^{loxP/loxP}$*; NPHS2-Cre* murine model. Our previous study showed that Tmem30a expression decreased in patients with minimal change disease and membranous nephropathy, and that *Tmem30a*$^{loxP/loxP}$*; NPHS2-Cre* mice eventually developed FSGS.[12] However, the specific effects and mechanisms of Tmem30a in podocyte injury remain unclear. Then, to further elucidate the specific effects and mechanisms of Tmem30a in podocyte injury, we performed bioinformatic analysis of FSGS-related GSE121233 and GSE129973 datasets. And we identified that the expression of Tmem30a was obviously reduced in FSGS patients following fold change ≥ |1.2| and adj. $p < 0.05$. Similarly, immunofluorescence showed that Tmem30a expression was downregulated in patients with FSGS and ADR-induced models compared with that in the control group. Consequently, this study examined how Tmem30a participates in podocyte injury.

The potential mechanisms of podocyte injury include glucose and lipid metabolism disorders, hypertension, renin angiotensin system (RAS) activation, microinflammation, and immune disorders.[29] Transmission electron microscopy showed that multiple pores formed in the membrane of podocytes from patients with FSGS, suggesting the occurrence of pyroptosis. Additionally, Tmem30a and nephrin expression levels were significantly downregulated in the glomerulus of patients with FSGS, ADR-induced mice, and *Tmem30a*$^{loxP/loxP}$*; NPHS2-Cre* mice; whereas the expression of NLRP3 and ASC were significantly upregulated. Our analysis of the GSE124622 dataset also demonstrated that pyroptosis plays an important role in ADR-induced podocyte injury. Pyroptosis is a type of programmed cell death that has been studied in several kidney diseases, including acute kidney injury and other chronic progressive diseases.[30,31] Our findings suggest that Tmem30a might be involved in podocyte injury by mediating pyroptosis.

NLRP3 is a well-studied inflammasome that activates caspase-1.[32] Activated caspase-1 cleaves GSDMD and activates IL-1β and IL-18, leading to podocyte pyroptosis.[33–35] ADR-induced mouse podocytes and *Tmem30a* KD mouse podocytes were used to mimic podocyte injury and explore the underlying mechanisms. Furthermore, MCC950 is a selective small molecule inhibitor of NLRP3 that blocks typical and atypical NLRP3 activation.[36] MCC950 has been reported to ameliorate proteinuria, renal histological lesions, and podocyte foot process effacement in lupus-prone mice.[37] For decades, DSF has been widely used to treat alcohol addiction by inhibiting aldehyde dehydrogenase.[38,39] Recently, DSF has been reported as an inhibitor of GSDMD-mediated pyroptosis, mainly by inhibiting inflammatory caspase activation, GSDMD expression, and GSDMD pore formation.[40–43] A recent study showed that DSF treatment could reduce proteinuria, serum anti-dsDNA levels and renal immune complex, and significantly inhibit pyroptosis in patients with systemic lupus erythematosus.[44] Therefore, we used MCC950 and DSF intervention in ADR-induced mouse podocytes and *Tmem30a* KD mouse podocytes. Notably, MCC950 and DSF effectively inhibited NLRP3 expression, cleavage of GSDMD, and the conversion of pro-caspase-1 and pro-IL-1β into their active forms. Additionally, MCC950 and DSF significantly increased the expression of the podocyte-associated molecules WT1 and nephrin in ADR-induced mouse podocytes and *Tmem30a* KD mouse podocytes. Overall, these findings indicate that MCC950 and DSF alleviate podocyte injury by inhibiting pyroptosis.

In conclusion, Tmem30a plays a protective role against pyroptosis in podocyte injury, making it a potential therapeutic target for podocyte injury in podocytopathies.

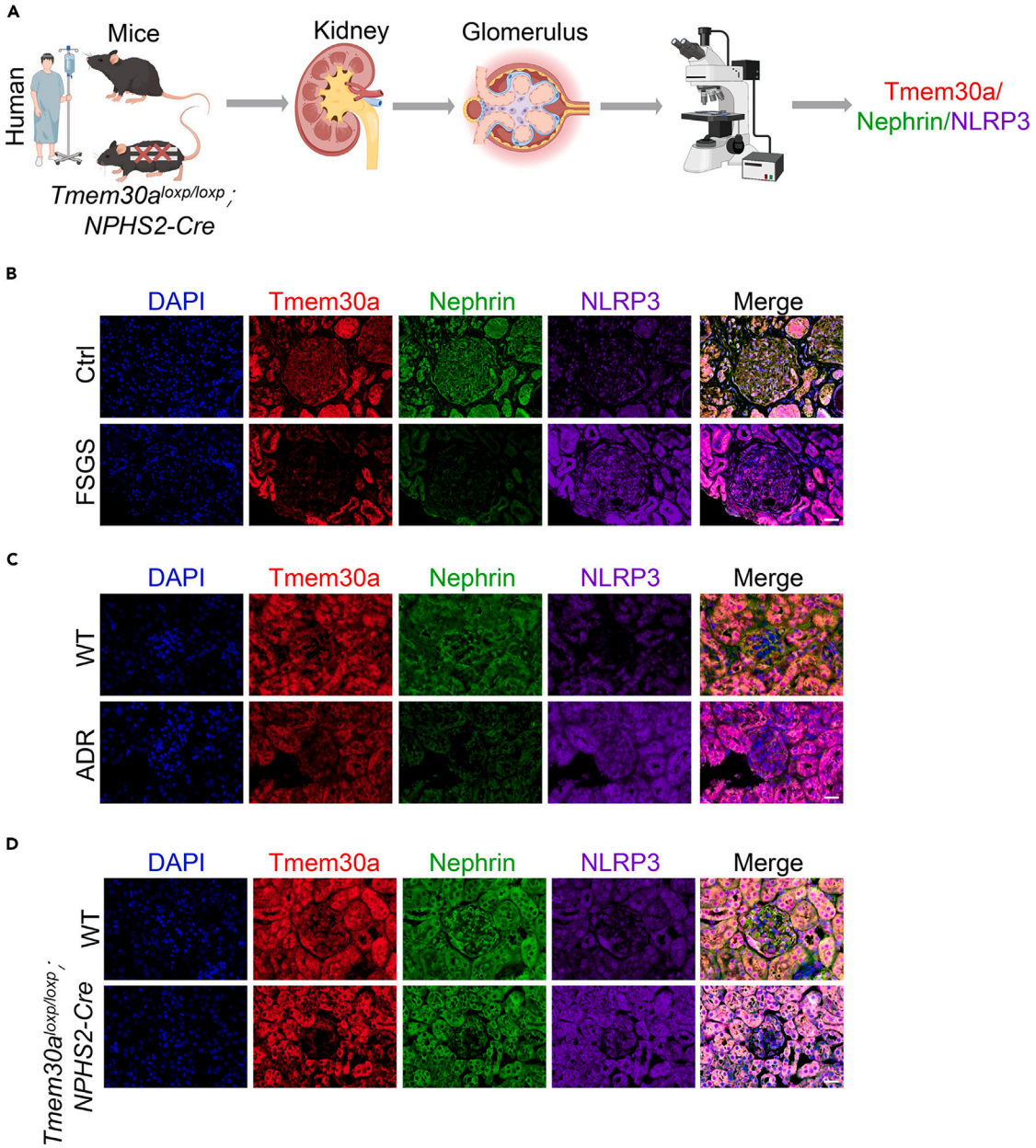

Figure 6. NLRP3 upregulation is observed in patients with FSGS, ADR-induced mice, and podocyte-specific *Tmem30a*$^{loxP/loxP}$; *NPHS2-Cre* mice

(A) Experimental design of multiplexed immunofluorescence staining.

(B) The expression levels of Tmem30a, nephrin, and NLRP3 in the glomeruli of FSGS group and Ctrl group using multispectral fluorescence staining (scale bar: 20 μm).

(C) The expression levels of Tmem30a, nephrin, and NLRP3 in the glomeruli of ADR-induced mice and WT mice using multispectral fluorescence staining (scale bar: 20 μm).

(D) The expression levels of Tmem30a, nephrin, and NLRP3 in the glomeruli of podocyte-specific *Tmem30a*$^{loxP/loxP}$; *NPHS2-Cre* mice and WT mice using multispectral fluorescence staining (scale bar: 20 μm). ADR, adriamycin; Ctrl, control; FSGS, focal segmental glomerulosclerosis; NLRP3, NLR family pyrin domain containing 3; Tmem30a, transmembrane protein 30a; WT, wild type.

Limitations of the study

Our study has some limitations. MCC950 is a potent and selective NLRP3 inhibitor but does not affect the AIM2, NLRC4, or NLRP1 inflammasomes. In addition, we only investigated the MCC950 and DSF mechanisms *in vitro*, and further studies are necessary to explore their role in patients with FSGS, the ADR-induced mouse model and podocyte-specific *Tmem30a*$^{loxP/loxP}$; *NPHS2-Cre* mouse model.

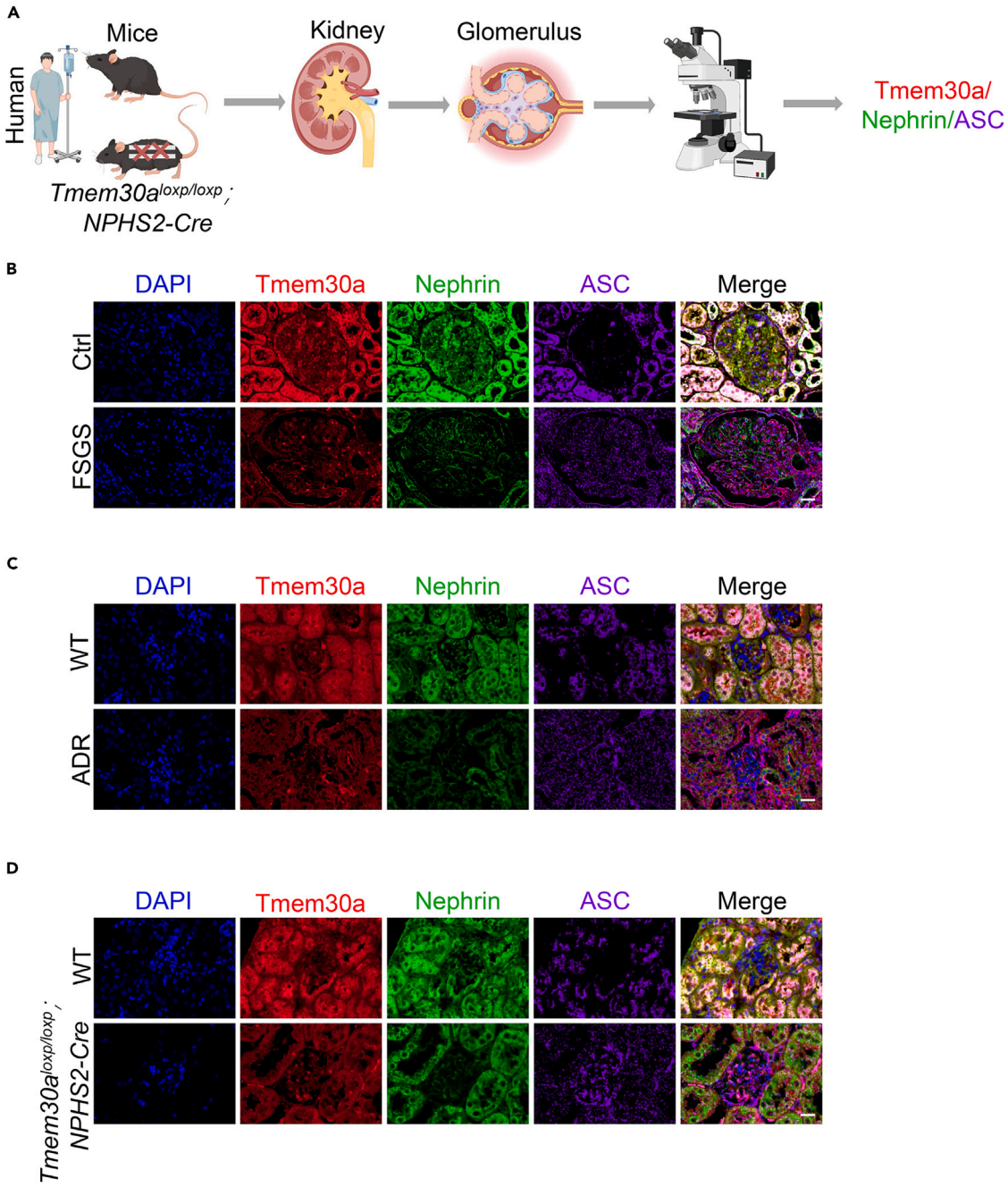

Figure 7. ASC upregulation is observed in patients with FSGS, ADR-induced podocyte injury mice, and podocyte-specific *Tmem30a*$^{loxP/loxP}$; *NPHS2-Cre* mice

(A) Experimental design of multiplexed immunofluorescence staining.

(B) The expression levels of Tmem30a, nephrin, and ASC in the glomeruli of FSGS group and Ctrl group using multispectral fluorescence staining (scale bar: 20 μm).

(C) The expression levels of Tmem30a, nephrin, and ASC in the glomeruli of ADR-induced mice and WT mice using multispectral fluorescence staining (scale bar: 20 μm).

(D) The expression levels of Tmem30a, nephrin, and ASC in the glomeruli of podocyte-specific *Tmem30a*$^{loxP/loxP}$; *NPHS2-Cre* mice and WT mice using multispectral fluorescence staining (scale bar: 20 μm). ADR, adriamycin; Ctrl, control; FSGS, focal segmental glomerulosclerosis; Tmem30a, transmembrane protein 30a; WT, wild type.

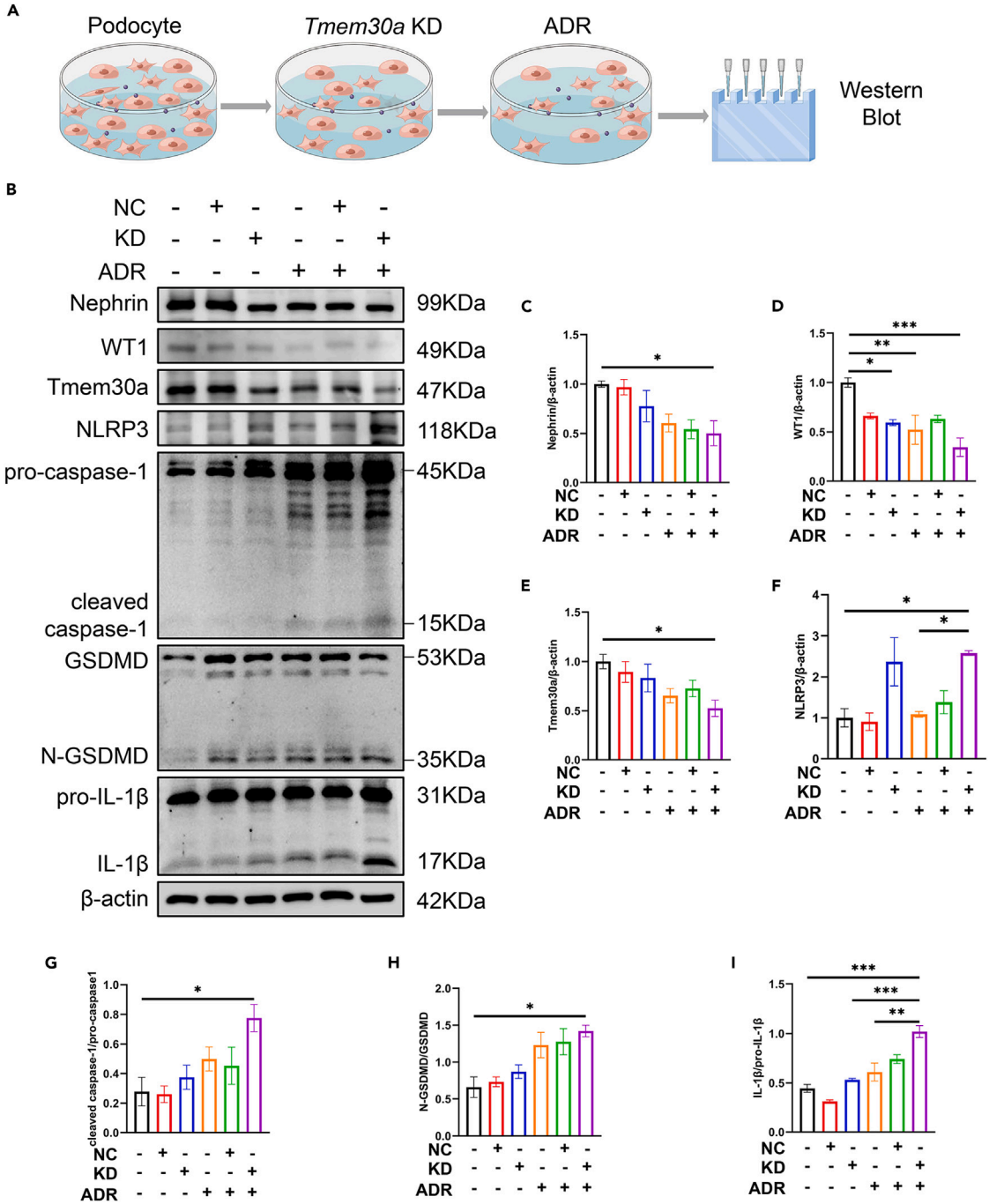

Figure 8. ADR aggravates podocyte injury and pyroptosis in *Tmem30a* KD mouse podocytes

(A) Experimental design for ADR intervention in *Tmem30a* KD mouse podocytes.

(B) Expression levels of nephrin, WT1, Tmem30a, NLRP3, pro-caspase-1, cleaved caspase-1, GSDMD, N-GSDMD, pro-IL-1β, and IL-1β in the Ctrl group, NC group, *Tmem30a* KD group, Ctrl + ADR group, NC + ADR group, and *Tmem30a* KD + ADR group using western blotting.

(C–I) Immunoblot quantification of nephrin, WT1, Tmem30a, NLRP3, cleaved caspase-1/pro-caspase-1, N-GSDMD/GSDMD, and IL-1β/pro-IL-1β in (B). n = 3/group. Data are represented as mean ± SEM. ADR, adriamycin; Ctrl, control; KD, knockdown; GSDMD, gasdermin D; NC, negative control; NLRP3, NLR family pyrin domain containing 3; Tmem30a, transmembrane protein 30a; WT1, Wilms tumor 1. *$p < 0.05$; **$p < 0.01$; ***$p < 0.001$.

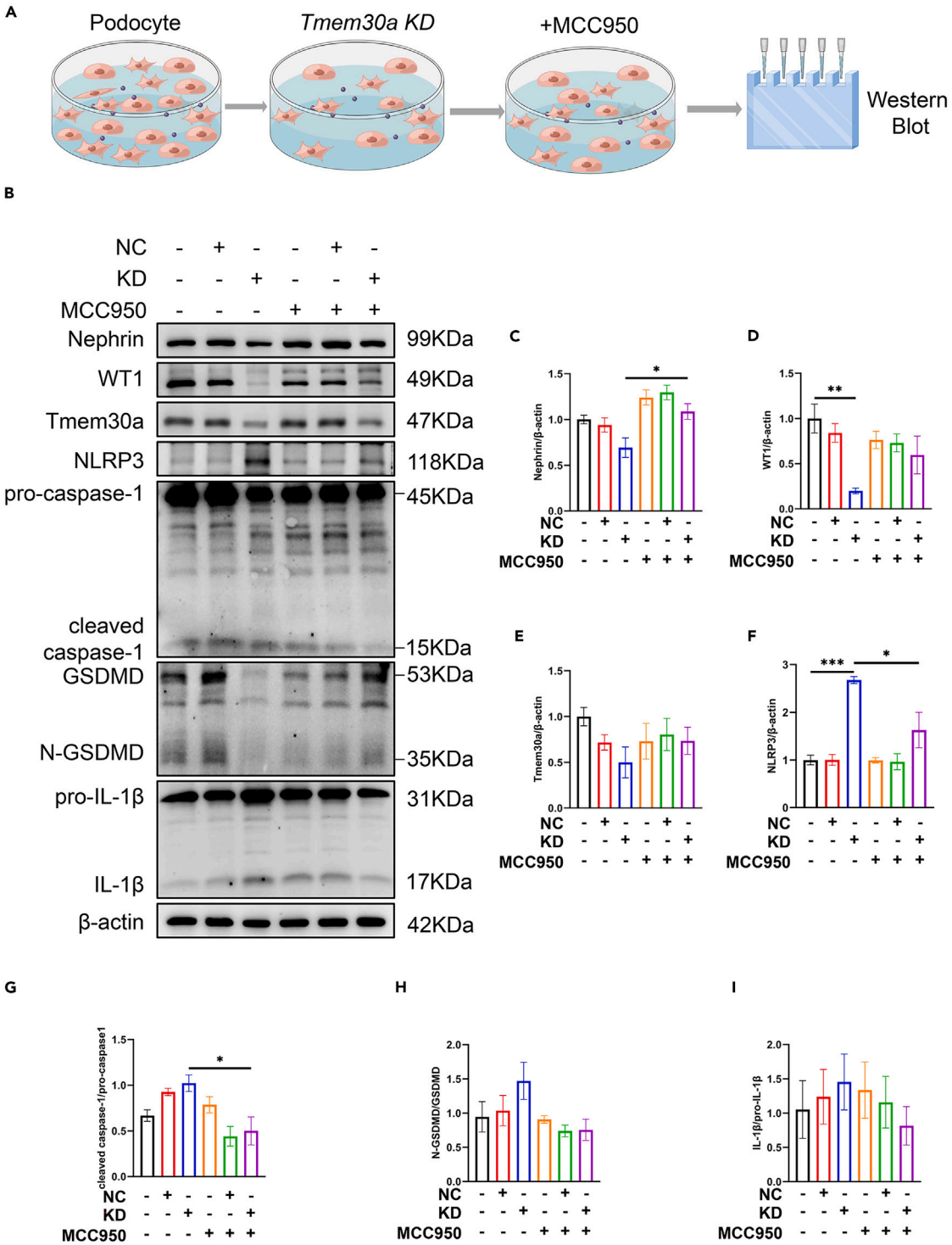

Figure 9. MCC950 alleviates podocyte injury by inhibiting *Tmem30a* KD induced pyroptosis

(A) Experimental design for MCC950 intervention in *Tmem30a* KD mouse podocytes.

(B) Expression levels of nephrin, WT1, Tmem30a, NLRP3, pro-caspase-1, cleaved caspase-1, GSDMD, N-GSDMD, pro-IL-1β, and IL-1β in the Ctrl group, NC group, *Tmem30a* KD group, Ctrl + MCC950 group, NC + MCC950 group, and *Tmem30a* KD + MCC950 group using western blotting.

(C–I) Immunoblot quantification of nephrin, WT1, Tmem30a, NLRP3, cleaved caspase-1/pro-caspase-1, N-GSDMD/GSDMD, and IL-1β/pro-IL-1β in (B). n = 3/group. Data are represented as mean ± SEM. Ctrl, control; NC, negative control; KD, knockdown; GSDMD, gasdermin D; NLRP3, NLR family pyrin domain containing 3; Tmem30a, transmembrane protein 30a; WT1, Wilms tumor 1. *$p < 0.05$; **$p < 0.01$; ***$p < 0.001$.

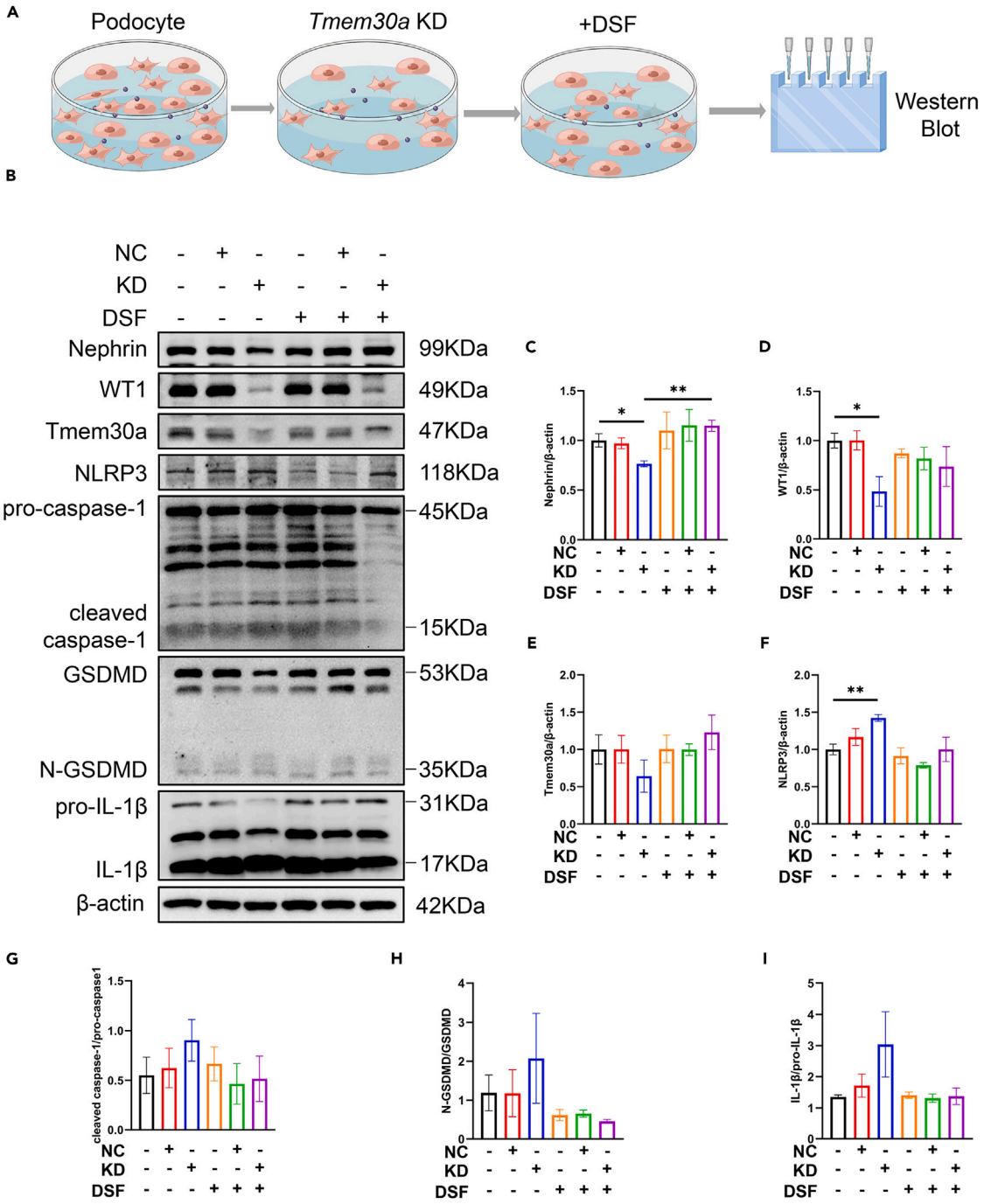

Figure 10. DSF alleviates podocyte injury by inhibiting *Tmem30a* KD induced pyroptosis

(A) Experimental design for DSF intervention in *Tmem30a* KD mouse podocytes.

(B) Expression levels of nephrin, WT1, Tmem30a, NLRP3, pro-caspase-1, cleaved caspase-1, GSDMD, N-GSDMD, pro-IL-1β, and IL-1β in the Ctrl group, NC group, *Tmem30a* KD group, Ctrl + DSF group, NC + DSF group, and *Tmem30a* KD + DSF group using western blotting.

(C–I) Immunoblot quantification of nephrin, WT1, Tmem30a, NLRP3, cleaved caspase-1/pro-caspase-1, N-GSDMD/GSDMD, and IL-1β/pro-IL-1β in (B). n = 3/group. Data are represented as mean ± SEM. Ctrl, control; NC, negative control; KD, knockdown; GSDMD, gasdermin D; NLRP3, NLR family pyrin domain containing 3; Tmem30a, transmembrane protein 30a; WT1, Wilms tumor 1. *$p < 0.05$; **$p < 0.01$.

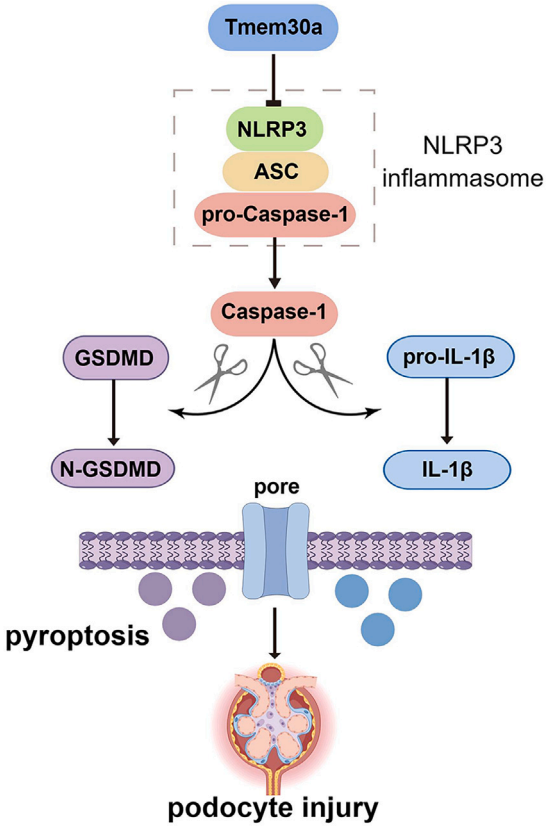

Figure 11. Diagram of the scientific hypotheses

Tmem30a, transmembrane protein 30a; NLRP3, NLR family pyrin domain containing 3.

STAR★METHODS

Detailed methods are provided in the online version of this paper and include the following:

- KEY RESOURCES TABLE
- RESOURCE AVAILABILITY
  - Lead contact
  - Materials availability
  - Data and code availability
- EXPERIMENTAL MODEL AND STUDY PARTICIPANT DETAILS
  - Cell culture
  - Mice models
  - Human subjects
- METHOD DETAILS
  - Construction of *Tmem30a* KD mouse podocytes
  - Bioinformatic analysis
  - Evaluation of urine and serum parameters
  - PAS and Masson's trichrome staining
  - Transmission electron microscopy
  - Immunohistochemistry staining
  - Immunofluorescence staining
  - Multiplexed immunofluorescence staining
  - Real Time-PCR
  - CCK-8 method
  - Western blot analysis
- QUANTIFICATION AND STATISTICAL ANALYSIS

SUPPLEMENTAL INFORMATION

Supplemental information can be found online at https://doi.org/10.1016/j.isci.2024.109976.

ACKNOWLEDGMENTS

This work was supported by projects from Department of Science and Technology of Sichuan Province (2021YFS0370, 2023ZYD0170, 2021YFS0372, and 24NSFSC1735), National Natural Science Foundation of China (82070690, U21A20349, 82270729, 8170742, 81700607, 82200767, and 81970641), Chengdu Science and Technology Bureau (2022-YF05-01940-SN), and Sichuan Provincial People's Hospital Post-doctoral fund (2022BH020). Some images in this article were drawn by Figdraw.

AUTHOR CONTRIBUTIONS

Conceptualization, G.L., Y.L., L.W., and X.Zhu; Methodology, Y.H. and W.L.; Software, L.H. and M.Y.; Validation, Y.H. and S.C.; Formal Analysis, L.P., Y.H., X.Zhong, and L.X; Investigation, H.Z. and P.Z; Resources, G.L., Y.L., L.W., and X.Zhu; Writing – Original Draft, Y.H. and Y.L.; Writing – Review & Editing, all authors; Visualization, Y.H.; Supervision, G.L. and Y.L.; Funding Acquisition, G.L., Y.L., L.W., L.P., X.Zhong, and Y.H.

DECLARATION OF INTERESTS

The authors declare no competing interests.

Received: October 16, 2023
Revised: April 6, 2024
Accepted: May 10, 2024
Published: May 14, 2024

REFERENCES

1. Ahn, W., and Bomback, A.S. (2020). Approach to Diagnosis and Management of Primary Glomerular Diseases Due to Podocytopathies in Adults: Core Curriculum 2020. Am. J. Kidney Dis. *75*, 955–964. https://doi.org/10.1053/j.ajkd.2019.12.019.
2. Kopp, J.B., Anders, H.J., Susztak, K., Podestà, M.A., Remuzzi, G., Hildebrandt, F., and Romagnani, P. (2020). Podocytopathies. Nat. Rev. Dis. Primers *6*, 68. https://doi.org/10.1038/s41572-020-0196-7.
3. Shankland, S.J. (2006). The podocyte's response to injury: Role in proteinuria and glomerulosclerosis. Kidney Int. *69*, 2131–2147. https://doi.org/10.1038/sj.ki.5000410.
4. Zeng, L., and Szeto, C.C. (2021). Urinary podocyte markers in kidney diseases. Clin. Chim. Acta *523*, 315–324. https://doi.org/10.1016/j.cca.2021.10.017.
5. Lopez-Marques, R., Gourdon, P., Gunther, T., and Palmgren, M. (2020). The transport mechanism of P4 ATPase lipid flippases. Biochem. J. *477*, 3769–3790. https://doi.org/10.1042/BCJ20200249.
6. Best, J.T., Xu, P., and Graham, T.R. (2019). Phospholipid flippases in membrane remodeling and transport carrier biogenesis. Curr. Opin. Cell Biol. *59*, 8–15. https://doi.org/10.1016/j.ceb.2019.02.004.
7. Hiraizumi, M., Yamashita, K., Nishizawa, T., and Nureki, O. (2019). Cryo-EM structures capture the transport cycle of the P4-ATPase flippase. Science *365*, 1149–1155. https://doi.org/10.1126/science.aay3353.
8. Yang, Y., Liu, W., Sun, K., Jiang, L., and Zhu, X. (2019). Tmem30a deficiency leads to retinal rod bipolar cell degeneration. J. Neurochem. *148*, 400–412. https://doi.org/10.1111/jnc.14643.
9. Liou, A.Y., Molday, L.L., Wang, J., Andersen, J.P., and Molday, R.S. (2019). Identification and functional analyses of disease-associated P4-ATPase phospholipid flippase variants in red blood cells. J. Biol. Chem. *294*, 6809–6821. https://doi.org/10.1074/jbc.RA118.007270.
10. Yang, Y., Sun, K., Liu, W., Zhang, L., Peng, K., Zhang, S., Li, S., Yang, M., Jiang, Z., Lu, F., and Zhu, X. (2018). Disruption of Tmem30a results in cerebellar ataxia and degeneration of Purkinje cells. Cell Death Dis. *9*, 899. https://doi.org/10.1038/s41419-018-0938-6.
11. Zhang, S., Liu, W., Yang, Y., Sun, K., Li, S., Xu, H., Yang, M., Zhang, L., and Zhu, X. (2019). Tmem30a deficiency in endothelial cells impairs cell proliferation and angiogenesis. J. Cell Sci. *132*, jcs225052. https://doi.org/10.1242/jcs.225052.
12. Liu, W., Peng, L., Tian, W., Li, Y., Zhang, P., Sun, K., Yang, Y., Li, X., Li, G., and Zhu, X. (2021). Loss of phosphatidylserine flippase beta-subunit Tmem30a in podocytes leads to albuminuria and glomerulosclerosis. Dis. Model. Mech. *14*, dmm048777. https://doi.org/10.1242/dmm.048777.
13. Segawa, K., Kurata, S., Yanagihashi, Y., Brummelkamp, T.R., Matsuda, F., and Nagata, S. (2014). Caspase-mediated cleavage of phospholipid flippase for apoptotic phosphatidylserine exposure. Science *344*, 1164–1168. https://doi.org/10.1126/science.1252809.
14. Yu, P., Zhang, X., Liu, N., Tang, L., Peng, C., and Chen, X. (2021). Pyroptosis: mechanisms and diseases. Signal. Transduct. Targeted Ther. *6*, 128. https://doi.org/10.1038/s41392-021-00507-5.
15. Shi, J., Gao, W., and Shao, F. (2017). Pyroptosis: Gasdermin-Mediated Programmed Necrotic Cell Death. Trends Biochem. Sci. *42*, 245–254. https://doi.org/10.1016/j.tibs.2016.10.004.
16. Liu, X., Zhang, Z., Ruan, J., Pan, Y., Magupalli, V.G., Wu, H., and Lieberman, J. (2016). Inflammasome-activated gasdermin D causes pyroptosis by forming membrane pores. Nature *535*, 153–158. https://doi.org/10.1038/nature18629.
17. Zhang, H., Deng, Z., Wang, Y., Zheng, X., Zhou, L., Yan, S., Wang, Y., Dai, Y., Kanwar, Y.S., and Deng, F. (2023). CHIP protects against septic acute kidney injury by inhibiting NLRP3-mediated pyroptosis. iScience *26*, 107762. https://doi.org/10.1016/j.isci.2023.107762.
18. Wang, K., Sun, Q., Zhong, X., Zeng, M., Zeng, H., Shi, X., Li, Z., Wang, Y., Zhao, Q., Shao, F., and Ding, J. (2020). Structural Mechanism for GSDMD Targeting by Autoprocessed Caspases in Pyroptosis. Cell *180*, 941–955.e20. https://doi.org/10.1016/j.cell.2020.02.002.
19. Shi, J., Zhao, Y., Wang, K., Shi, X., Wang, Y., Huang, H., Zhuang, Y., Cai, T., Wang, F., Shao, F., et al. (2015). Cleavage of GSDMD by inflammatory caspases determines pyroptotic cell death. Nature *526*, 660–665. https://doi.org/10.1038/nature15514.
20. Lin, Y., Lv, X., Sun, C., Sun, Y., Yang, M., Ma, D., Jing, W., Zhao, Y., Cheng, Y., Xuan, H., and Han, L. (2022). TRIM50 promotes NLRP3 inflammasome activation by directly inducing NLRP3 oligomerization. EMBO Rep. *23*, e54569. https://doi.org/10.15252/embr.202154569.
21. He, Y., Hara, H., and Núñez, G. (2016). Mechanism and Regulation of NLRP3 Inflammasome Activation. Trends Biochem. Sci. *41*, 1012–1021. https://doi.org/10.1016/j.tibs.2016.09.002.
22. Ding, J., Wang, K., Liu, W., She, Y., Sun, Q., Shi, J., Sun, H., Wang, D.C., and Shao, F. (2016). Pore-forming activity and structural autoinhibition of the gasdermin family. Nature *535*, 111–116. https://doi.org/10.1038/nature18590.

23. Broz, P., Pelegrín, P., and Shao, F. (2020). The gasdermins, a protein family executing cell death and inflammation. Nat. Rev. Immunol. *20*, 143–157. https://doi.org/10.1038/s41577-019-0228-2.
24. Swanson, K.V., Deng, M., and Ting, J.P.Y. (2019). The NLRP3 inflammasome: molecular activation and regulation to therapeutics. Nat. Rev. Immunol. *19*, 477–489. https://doi.org/10.1038/s41577-019-0165-0.
25. Li, Y., Xia, W., Wu, M., Yin, J., Wang, Q., Li, S., Zhang, A., Huang, S., Zhang, Y., and Jia, Z. (2020). Activation of GSDMD contributes to acute kidney injury induced by cisplatin. Am. J. Physiol. Renal Physiol. *318*, F96–F106. https://doi.org/10.1152/ajprenal.00351.
26. Cao, H., Liang, J., Liu, J., He, Y., Ke, Y., Sun, Y., Jiang, S., and Lin, J. (2021). Novel Effects of Combination Therapy Through Inhibition of Caspase-1/Gasdermin D Induced-Pyroptosis in Lupus Nephritis. Front. Immunol. *12*, 720877. https://doi.org/10.3389/fimmu.2021.720877.
27. Haque, S., Lan, X., Wen, H., Lederman, R., Chawla, A., Attia, M., Bongu, R.P., Husain, M., Mikulak, J., Saleem, M.A., et al. (2016). HIV Promotes NLRP3 Inflammasome Complex Activation in Murine HIV-Associated Nephropathy. Am. J. Pathol. *186*, 347–358. https://doi.org/10.1016/j.ajpath.2015.10.002.
28. Cellesi, F., Li, M., and Rastaldi, M.P. (2015). Podocyte injury and repair mechanisms. Curr. Opin. Nephrol. Hypertens. *24*, 239–244. https://doi.org/10.1097/MNH.0000000000000124.
29. Lu, C.C., Wang, G.H., Lu, J., Chen, P.P., Zhang, Y., Hu, Z.B., and Ma, K.L. (2019). Role of Podocyte Injury in Glomerulosclerosis. Adv. Exp. Med. Biol. *1165*, 195–232. https://doi.org/10.1007/978-981-13-8871-2_10.
30. Miao, N., Yin, F., Xie, H., Wang, Y., Xu, Y., Shen, Y., Xu, D., Yin, J., Wang, B., Zhou, Z., et al. (2019). The cleavage of gasdermin D by caspase-11 promotes tubular epithelial cell pyroptosis and urinary IL-18 excretion in acute kidney injury. Kidney Int. *96*, 1105–1120. https://doi.org/10.1016/j.kint.2019.04.035.
31. Peng, X., Yang, T., Liu, G., Liu, H., Peng, Y., and He, L. (2018). Piperine ameliorated lupus nephritis by targeting AMPK-mediated activation of NLRP3 inflammasome. Int. Immunopharmacol. *65*, 448–457. https://doi.org/10.1016/j.intimp.2018.10.025.
32. Vanaja, S.K., Rathinam, V.A.K., and Fitzgerald, K.A. (2015). Mechanisms of inflammasome activation: recent advances and novel insights. Trends Cell Biol. *25*, 308–315. https://doi.org/10.1016/j.tcb.2014.12.009.
33. Ding, X., Jing, N., Shen, A., Guo, F., Song, Y., Pan, M., Ma, X., Zhao, L., Zhang, H., Wu, L., et al. (2021). MiR-21-5p in macrophage-derived extracellular vesicles affects podocyte pyroptosis in diabetic nephropathy by regulating A20. J. Endocrinol. Invest. *44*, 1175–1184. https://doi.org/10.1007/s40618-020-01401-7.
34. He, W.T., Wan, H., Hu, L., Chen, P., Wang, X., Huang, Z., Yang, Z.H., Zhong, C.Q., and Han, J. (2015). Gasdermin D is an executor of pyroptosis and required for interleukin-1β secretion. Cell Res. *25*, 1285–1298. https://doi.org/10.1038/cr.2015.139.
35. Schneider, K.S., Groß, C.J., Dreier, R.F., Saller, B.S., Mishra, R., Gorka, O., Heilig, R., Meunier, E., Dick, M.S., Ćiković, T., et al. (2017). The Inflammasome Drives GSDMD-Independent Secondary Pyroptosis and IL-1 Release in the Absence of Caspase-1 Protease Activity. Cell Rep. *21*, 3846–3859. https://doi.org/10.1016/j.celrep.2017.12.018.
36. Coll, R.C., Robertson, A.A.B., Chae, J.J., Higgins, S.C., Muñoz-Planillo, R., Inserra, M.C., Vetter, I., Dungan, L.S., Monks, B.G., Stutz, A., et al. (2015). A small-molecule inhibitor of the NLRP3 inflammasome for the treatment of inflammatory diseases. Nat. Med. *21*, 248–255. https://doi.org/10.1038/nm.3806.
37. Fu, R., Guo, C., Wang, S., Huang, Y., Jin, O., Hu, H., Chen, J., Xu, B., Zhou, M., Zhao, J., et al. (2017). Podocyte Activation of NLRP3 Inflammasomes Contributes to the Development of Proteinuria in Lupus Nephritis. Arthritis Rheumatol. *69*, 1636–1646. https://doi.org/10.1002/art.40155.
38. Chick, J., Gough, K., Falkowski, W., Kershaw, P., Hore, B., Mehta, B., Ritson, B., Ropner, R., and Torley, D. (1992). Disulfiram treatment of alcoholism. Br. J. Psychiatry *161*, 84–89. https://doi.org/10.1192/bjp.161.1.84.
39. Wright, C., and Moore, R.D. (1990). Disulfiram treatment of alcoholism. Am. J. Med. *88*, 647–655. https://doi.org/10.1016/0002-9343(90)90534-k.
40. Zhang, J., Dai, Y., Yang, Y., and Xu, J. (2021). Calcitriol Alleviates Hyperosmotic Stress-Induced Corneal Epithelial Cell Damage via Inhibiting the NLRP3-ASC-Caspase-1-GSDMD Pyroptosis Pathway in Dry Eye Disease. J. Inflamm. Res. *14*, 2955–2962. https://doi.org/10.2147/JIR.S310116.
41. Hu, J.J., Liu, X., Xia, S., Zhang, Z., Zhang, Y., Zhao, J., Ruan, J., Luo, X., Lou, X., Bai, Y., et al. (2020). FDA-approved disulfiram inhibits pyroptosis by blocking gasdermin D pore formation. Nat. Immunol. *21*, 736–745. https://doi.org/10.1038/s41590-020-0669-6.
42. Tian, J., Wang, B., Xie, B., Liu, X., Zhou, D., Hou, X., and Xiang, L. (2022). Pyroptosis inhibition alleviates potassium oxonate- and monosodium urate-induced gouty arthritis in mice. Mod. Rheumatol. *32*, 221–230. https://doi.org/10.1080/14397595.2021.1899569.
43. Zhang, Y., Zhang, R., and Han, X. (2021). Disulfiram inhibits inflammation and fibrosis in a rat unilateral ureteral obstruction model by inhibiting gasdermin D cleavage and pyroptosis. Inflamm. Res. *70*, 543–552. https://doi.org/10.1007/s00011-021-01457-y.
44. Zhuang, L., Luo, X., Wu, S., Lin, Z., Zhang, Y., Zhai, Z., Yang, F., Li, Y., Zhuang, J., Luo, G., et al. (2022). Disulfiram alleviates pristane-induced lupus via inhibiting GSDMD-mediated pyroptosis. Cell Death Discov. *8*, 379. https://doi.org/10.1038/s41420-022-01167-2.

STAR★METHODS

KEY RESOURCES TABLE

REAGENT or RESOURCE	SOURCE	IDENTIFIER
Antibodies		
Rabbit polyclonal anti-Tmem30a	Bioss	Cat# bs-16576R-1
Rabbit polyclonal anti-Nephrin	Novusbio	Cat# NBP1-77303, RRID: AB_11040198
Rabbit polyclonal anti-NLRP3	Abcam	Cat# ab214185, RRID: AB_2819003
Rabbit polyclonal anti-WT1	Proteintech	Cat# 12609-1-AP, RRID: AB_2216225
Rabbit monoclonal anti-pro Caspase-1+p10+p12 antibody	Abcam	Cat# ab179515, RRID: AB_2884954
Rabbit monoclonal anti-GSDMD	Abcam	Cat# ab209845, RRID: AB_2783550
Rabbit polyclonal anti-IL-1β	ZEN BIO	Cat# 516288, Lot# MO8FE01, RRID: AB_2934281
Rabbit polyclonal anti-IL-1β	ZEN BIO	Cat# 516288, Lot# M26AP01, RRID: AB_2934281
Rabbit polyclonal anti-ASC/TMS1 antibody	Proteintech	Cat# 10500-1-AP, RRID: AB_2174862
Goat Anti-Rabbit IgG H&L (HRP)	ZEN BIO	Cat# 511203, RRID: AB_2927753
Goat Anti-Rabbit IgG H&L (Alexa Fluor® 488)	Abcam	Cat# ab150077, RRID: AB_2630356
Beta Actin (8F10) Mouse mAb (HRP)	ZEN BIO	Cat# 700068
Biological samples		
Human: renal tissue samples of primary FSGS patients	This paper	N/A
Human: renal tissue samples of IgAN patients	This paper	N/A
Human: renal tissue samples of healthy controls	This paper	N/A
Chemicals, peptides, and recombinant proteins		
Fetal bovine serum	Gibco	Cat# 10099-141C
RPMI 1640 medium	Gibco	Cat# C11875500BT
Penicillin-Streptomycin Solution	Hyclone	Cat# SV30010
Recombinant mouse γ-interferon	Chamot Biotechnology	Cat# CM052
ADR	Selleck	Cat# S1208
MCC950	Selleck	Cat# S7809
DSF	Selleck	Cat# S1680
Normal saline	Solarbio	Cat# IN9000
Trizol reagent	Invitrogen	Cat# 15596026
DAB chromogenic liquid	ZSGB-BIO	Cat# ZLI-9018
Antigen retrieval buffer solution (pH 8)	ZSGB-BIO	Cat# ZLI-9072
Pepsase	ZSGB-BIO	Cat# ZLI-9013
Normal goat serum	Solarbio	Cat# SL038
4′,6-diamidino-2-phenylindole (DAPI)	Solarbio	Cat# C0065
Phosphate Buffered Saline	Hyclone	Cat# SH3025601
RIPA Lysis Buffer	Beyotime	Cat# P0013B
SDS-PAGE protein Loading buffer (5X)	Beyotime	Cat# P1040
Albumin Bovine V (BSA-V)	Solarbio	Cat# A8020

(*Continued on next page*)

Continued

REAGENT or RESOURCE	SOURCE	IDENTIFIER
Skim Milk	Solarbio	Cat# D8340
SDS	Solarbio	Cat# S8010
TBS	Biohao	Cat# P0430
Tris	Solarbio	Cat# T8060
Methyl Alcohol	Chronchem	Cat# 67-56-1
Glycine	Solarbio	Cat# G8200
Hypersensitive ECL Western HRP Substrate	ZEN BIO	Cat# 17046
Trypsin	Hyclone	Cat# SH30042.01
Dimethyl sulfoxide	MP biomedical	Cat# 0219605580
Formaldehyde Solution	Chronchem	Cat# 50-00-0
Prestained Protein Marker	Mei5bio	Cat# MF028–PLUS-01; MF028-01
3-color Prestained Protein Marker	ZEN BIO	Cat# 17002
Phenylmethanesulfonyl fluoride	Beyotime	Cat# ST506
CCK-8	oriscience	Cat# CB101
PVDF Membrane	MIllipore	Cat# IPVH00010
Gluta fixative	Solarbio	Cat# P1126
RNase-free water	TIANGEN	Cat# RT121-02
Critical commercial assays		
PrimeScript RT Reagent Kit	TaKaRa	Cat# RR047A
TB Green Premix Ex Taq II kit	TaKaRa	Cat# RR820A
Opal 4-Color Manual IHC staining Kit	Akoya Bioscience	Cat# NEL810001KT
BCA protein concentration determination kit	Biosharp	Cat# BL521A
Creatinine Assay kits	Nanjing Jiancheng	Cat# C011-2-1
PAS staining kit	Solarbio	Cat# G1285
Modified Masson three-color dyeing kit	Solarbio	Cat# G1346
Urine protein test kits	Nanjing Jiancheng	Cat# C035-2-1
Deposited data		
Raw and analyzed data	This paper	N/A
GSE121233, GSE129973, and GSE124622 microarray datasets	GEO database of the National Center for Biotechnology Information (NCBI)	https://www.ncbi.nlm.nih.gov/geo/
Experimental models: Cell lines		
Mice: Immortalized mouse podocytes	General Hospital of Nanjing Military Region	N/A
Experimental models: Organisms/strains		
Mice: C57BL/6	Vital River	N/A
Mice: podocyte-specific *Tmem30a*$^{loxp/loxp}$; *NPHS2-Cre* mice	Donated by Zhu Xianjun	N/A
Oligonucleotides		
Random primers	TaKaRa	Cat# RR037A
Primer: β-actin-F (GCACTGTGTTGGCA TAGAGGTCTT) and β-actin-R (TCACTA TTGGCAACGAGCGGTTC)	This paper	N/A
Primer: Tmem30a-F (AATGATCAACTGT AATTCCCC) and Tmem30a-R (ATTCCC CTCAAGATAGCTAC)	This paper	N/A
Tmem30a Interference with the lentivirus	Jikai gene	N/A

(*Continued on next page*)

Continued

REAGENT or RESOURCE	SOURCE	IDENTIFIER
Software and algorithms		
ImageJ	National Institutes of Health	https://mirror.imagej.net
SPSS software (version 25.0)	SPSS Inc.	https://www.ibm.com/support/pages/downloading-ibm-spss-statistics-25
GraphPad Prism (version 9.3.1)	GraphPad Software	https://www.graphpad.com

RESOURCE AVAILABILITY

Lead contact

Further information and any reasonable request for data generated and/or used in this study should be directed to the lead contact, Guisen Li (guisenli@163.com).

Materials availability

This study did not generate new unique reagents.

Data and code availability

- The deposited data of this study are presented in key resources table. All data reported in this paper will be shared by the lead contact upon reasonable request.
- This paper does not report original code.
- Any additional information required to reanalyze the data reported in this paper is available from the lead contact upon reasonable request.

EXPERIMENTAL MODEL AND STUDY PARTICIPANT DETAILS

Cell culture

Immortalized mouse podocytes were donated to our laboratory by the General Hospital of Nanjing Military Region, which were cultured in RPMI 1640 medium containing 10% fetal bovine serum (Gibco), 1% penicillin/streptomycin, and 20 U/mL recombinant mouse γ-interferon (Chamot Biotechnology) at 33°C in a 5% CO_2 incubator. Thereafter, mature podocytes were transferred to a medium without recombinant mouse γ-interferon to induce podocyte differentiation for approximately 10–14 days and incubated at 37°C with 5% CO_2. The podocytes were passaged at approximately 80% confluency. Podocytes were treated with 0.4 μg/mL of ADR (Selleck, China) or blank vehicle for 24 h. They were then treated with 100 μM of the NLRP3 inhibitor MCC950 (Selleck) for another 48 h or 300 nM of the GSDMD inhibitor DSF (Selleck) for 1 h prior to model.

Mice models

The animal experimentation scheme was approved by the Institutional Animal Care and Use Committee of the Sichuan Academy of Medical Sciences, Sichuan Provincial People's Hospital, School of Medicine, University of Electronic Science and Technology of China. All experiments were conducted in accordance with the National Institutes of Health Guide for the Care and Use of Laboratory Animals. WT male C57BL/6J mice (8-week-old) were housed in a controlled environment (temperature, 20–26°C; humidity, 40–70%) under a 12 h light/dark cycle and had *ad libitum* access to food and water. After 7 days of adaptation, the experimental and control groups were injected with ADR and saline through the tail vein, respectively. After 16 weeks, the animals were humanely euthanized after collecting blood. Additionally, we generated podocyte-specific *Tmem30a*$^{loxP/loxP}$*; NPHS2-Cre* mice following previously described procedures.[12] After 5 months, the podocyte-specific *Tmem30a*$^{loxP/loxP}$*; NPHS2-Cre* mice were euthanized before further experimentation.

Human subjects

In this study, we collected patients aged 18-60 years old, ethnic Han, regardless of gender, who were admitted to the Sichuan People's Hospital from 2019 to 2023. And renal tissue samples were collected from ten patients with primary FSGS and five with non-segmental glomerulosclerosis IgAN as disease controls. Five normal tissue samples collected near the cancer site were used as controls. This study was approved by the Ethics Committee of Sichuan Provincial People's Hospital and the University of Electronic Science and Technology Hospital in China (No. 2020. 224) in accordance with the Declaration of Helsinki. All participants signed informed consent.

METHOD DETAILS

Construction of *Tmem30a* KD mouse podocytes

Tmem30a was knocked down in immortalized mouse podocytes using lentivirus-mediated RNA interference, and phenotypic analysis and functional verification were performed at the cellular level. Cells were transfected for 72 h with the interfering virus, after which Tmem30a knockdown was verified using RT-PCR and western blotting. Differentiated podocytes (control group), transfected negative control lentivirus mouse podocytes (NC group), and *Tmem30a* KD mouse podocytes (*Tmem30a* KD group) were treated with 0.4 μg/mL of ADR for 24 h. They were then treated with 100 μM of the NLRP3 inhibitor MCC950 (Selleck) for another 48 h or 300 nM of the GSDMD inhibitor DSF (Selleck) for 1 h prior to model.

Bioinformatic analysis

Podocyte injury-related datasets were retrieved from the GEO database of the National Center for Biotechnology Information. After careful screening, we selected GSE121233, GSE129973, and GSE124622 microarray datasets, which met the screening criteria. The microarray data were calibrated and normalized using R, and DEGs were identified using the R software package "*limma*." The DEGs were considered significant at fold change $\geq |1.2|$ and adj. $P < 0.05$.

Evaluation of urine and serum parameters

Mice urine samples were collected in metabolic cages for 24 h before euthanasia. Urinary creatinine and albumin levels were determined using creatinine and urine protein test kits (Cat#: C011-2-1; C035-2-1, Nanjing Jiancheng Bioengineering Institute), respectively, following the manufacturer's instructions. Urinary protein values were standardized against urine creatinine values of the same individuals.

PAS and Masson's trichrome staining

Renal tissues were fixed in 4% formalin, dehydrated, embedded, and cut into 2-μm sections. A PAS staining kit (G1285, Solarbio, China) was used according to the manufacturer's instructions. Briefly, renal tissue sections were incubated with a periodic acid solution for 15 min, washed with ddH2O, and then incubated with Schiff's reagent for 1 h at 37°C in the dark. The sections were counterstained with hematoxylin and eosin for 5 min. According to the modified Masson's three-color dyeing kit (G1346, Solarbio, China), each section was stained with hematoxylin solution for 15 min, washed, and differentiated for several seconds using a differentiation solution. Ponceau magenta stain liquid was then added for 10 min. A phosphomolybdic acid solution was added to the sections, and then an aniline blue dye solution was applied for 2 min, and the sections were washed. Neutral gum was used to seal the sections before they were imaged using a microscope (Cat#: BX53F, Olympus, Japan).

Transmission electron microscopy

Renal tissues were fixed in 1% osmic acid, dehydrated in an alcohol and acetone gradient, embedded in acetone and 812 embedding agents, polymerized in an oven at 60°C, and sliced into sections using an ultra-thin microtome. The copper mesh was further stained, and the sections were observed using a transmission electron microscope (Cat#: JEM-1400 PLUS, Japan).

Immunohistochemistry staining

Immunohistochemistry was performed on 2-μm thick sections of paraffin-embedded kidney tissue samples to detect the protein expression of Tmem30a. Briefly, paraffin-embedded kidney tissue samples were dewaxed, rehydrated in water, and heat-induced antigen retrieval for 3 min using buffer solution (pH 8) in a pressure cooker. Thereafter, the slides were blocked with 3% hydrogen peroxide for 30 min, followed by incubation with Tmem30a antibody (Cat#: bs-16576R-1, Bioss, 1:300) overnight at 4°C then with a secondary anti-rabbit IgG antibody for 30 min at room temperature. Finally, the sections were stained with 3, 3′-diaminobenzidine for color development, and images were captured using a digital microscope slide scanner (Cat#: VS200, Olympus, Japan).

Immunofluorescence staining

Paraffin-embedded kidney tissue samples were cut into 2-μm thick sections, dewaxed, rehydrated, heat-induced antigen retrieval buffer solution (pH 8), and permeabilized with pepsase for 6 min. Thereafter, the sections were blocked with 10% normal goat serum for 30 min, followed by incubation with rabbit anti-Tmem30a (Cat#: bs-16576R-1, Bioss, 1:300) overnight at 4°C and further incubation with a goat anti-rabbit secondary antibody at room temperature for 1 h. Finally, the nuclei were stained with 4′,6-diamidino-2-phenylindole (DAPI, Solarbio, C0065), and images were captured using a fluorescence microscope (Zeiss LSM980 Airyscan 2, Germany).

Multiplexed immunofluorescence staining

Multiplexed immunofluorescence staining was performed using the Opal Multiplex IHC kit (Akoya Biosciences, USA). Paraffin-embedded kidney tissue samples were cut into 2-μm thick sections, baked, dewaxed, and rehydrated in water. High-intensity epitope retrieval was performed using either AR6 or AR9 buffers. The following five steps were followed consecutively for each marker: incubate tissue with blocking solution at room temperature for 10 min; incubated with primary antibody; incubate with secondary antibody HRP conjugate for 10 min at

room temperature; incubate with an opal fluorophore for 10 min at room temperature; rinse slides with AR6 or AR9, using a microwave-safe slide jar, perform microwave treatments. Incubate with DAPI for 5 min at room temperature. The primary antibodies were as follows: rabbit anti-Tmem30a (Cat#: bs-16576R-1, Bioss,1:300), rabbit anti-Nephrin (Cat#: NBP1-77303, Novusbio, 1:200), rabbit anti-ASC (Cat#: 10500-1-AP, Proteintech, 1:200), and rabbit anti-NLRP3 (Cat#: ab214185, Abcam, 1:200). Images were captured using a fluorescence microscope.

Real Time-PCR

Total RNA was isolated using TRIzol reagent and reverse-transcribed using a PrimeScript RT reagent kit (RR047A, TaKaRa, China) on a GeneAmp PCR System (9700, ABI, USA). RT-PCR was performed using a TB Green Premix Ex Taq II kit (RR820A, TaKaRa) on a CFX96 Real-Time PCR Detection System (CFX96 Touch, Bio-Rad). The relative mRNA fold changes were calculated using the $2^{-\Delta\Delta Ct}$ method, and β-actin expression was used to standardize the results. The primer sequences are as follows: β-actin-F (GCACTGTGTTGGCATAGAGG TCTT) and β-actin-R (TCACTATTGGCAACGAGCGGTTC), and Tmem30a-F (AATGATCAACTGTAATTCCCC) and Tmem30a-R (ATTCCC CTCAAGATAGCTAC).

CCK-8 method

The cells (5×10^3 cells/well) were plated in 96-well plates and corresponding interventions were carried out. Then, 10 μL of CCK-8 solution (Cat#: CB101, Oriscience) was added to each well, and the plates were incubated for another 2 h at 37°C. The optical density at 450 nm was measured using a microplate reader (SpectraMax i3x).

Western blot analysis

Mouse podocytes were lysed using a mixture of RIPA buffer (Cat#: P0013B, Beyotime) and protease inhibitor phenylmethanesulfonyl fluoride (Cat#: ST506, Beyotime). Protein concentrations were quantified using the BCA protein concentration determination kit (Cat#: BL521A, Biosharp). Proteins were separated using 10, 12.5, or 15% sodium dodecyl sulfate-polyacrylamide gel electrophoresis and transferred to immobilon-P polyvinylidene difluoride membranes. The membranes were blocked with 5% nonfat milk or 5% bovine serum albumin in Tris buffered-saline with Tween 20 for 2 h and then incubated overnight at 4°C with the following primary antibodies: rabbit anti-Tmem30a (Cat#: bs-16576R-1, Bioss, 1:1000), rabbit anti-Nephrin (Cat#: NBP1-77303, Novusbio, 1:2000), rabbit anti-WT1 (Cat#: 12609-1-AP, Proteintech, 1:500), rabbit anti-NLRP3 (Cat#: ab214185, Abcam, 1:500), rabbit anti caspase-1 (Cat#: ab179515, Abcam, 1:1000), rabbit anti-GSDMD (Cat#: ab209845, Abcam, 1:1000), and rabbit anti-IL-1β (Cat#: 516288, ZEN BIO, 1:1000). Thereafter, the membranes were incubated with horseradish peroxidase-conjugated goat anti-rabbit secondary antibody at a dilution ratio of 1:10,000 for 2 h. Signals were detected using a fully automatic chemiluminescent gel imaging system (OI600; China). Densitometry was performed using Image J software.

QUANTIFICATION AND STATISTICAL ANALYSIS

GraphPad Prism (version 9.3.1, GraphPad Software, USA) was used for the statistical analyses. All data were expressed as mean ± standard error of the mean (SEM). Between-group comparisons of normally distributed data were performed using a Student's *t*-test, whereas Mann–Whitney U tests were used non-normally distributed data. One-way analysis of variance was used for comparisons among more than two groups. Statistical significance was set at $P < 0.05$.